PERGAMON

Acta mater. 48 (2000) 279–306

Acta MATERIALIA

www.elsevier.com/locate/actamat

STABILIZATION OF METALLIC SUPERCOOLED LIQUID AND BULK AMORPHOUS ALLOYS*

AKIHISA INOUE

Institute for Materials Research, Tohoku University, Sendai 980-8577, Japan

(Received 1 June 1999; accepted 15 July 1999)

Abstract—Bulk metallic materials have ordinarily been produced by melting and solidification processes for the last several thousand years. However, metallic liquid is unstable at temperatures below the melting temperature and solidifies immediately into crystalline phases. Consequently, all bulk engineering alloys are composed of a crystalline structure. Recently, this common concept was exploded by the findings of the stabilization phenomenon of the supercooled liquid for a number of alloys in the Mg-, lanthanide-, Zr-, Ti-, Fe-, Co-, Pd–Cu- and Ni-based systems. The alloys with the stabilized supercooled liquid state have three features in their alloy components, i.e. multicomponent systems, significant atomic size ratios above 12%, and negative heats of mixing. The stabilization mechanism has also been investigated from experimental data of structure analyses and fundamental physical properties. The stabilization has enabled the production of bulk amorphous alloys in the thickness range of 1–100 mm by using various casting processes. Bulk amorphous Zr-based alloys exhibit high mechanical strength, high fracture toughness and good corrosion resistance and have been used for sporting goods materials. The stabilization also leads to the appearance of a large supercooled liquid region before crystallization and enables high-strain rate superplasticity through Newtonian flow. The new Fe- and Co-based amorphous alloys exhibit a large supercooled liquid region and good soft magnetic properties which are characterized by low coercive force and high permeability. Furthermore, homogeneous dispersion of nanoscale particles into Zr-based bulk amorphous alloys was found to cause an improvement of tensile strength without detriment to good ductility. The discovery of the stabilization phenomenon, followed by the clarification of the stabilization criteria of the supercooled liquid, will promise the future definite development of bulk amorphous alloys as new basic science and engineering materials.

Keywords: Supercooled liquids; Amorphous materials; Metallic glasses; Stability; Microstructure

1. HISTORY AND ALLOY COMPONENTS OF BULK AMORPHOUS ALLOYS

Since the first synthesis of an amorphous phase in the Au–Si system by a rapid solidification technique in 1960 [1], a great number of amorphous alloys has been produced for the last three decades. It is well known that Fe-, Co- and Ni-based amorphous alloys found before 1990 require high cooling rates above 10^5 K/s for glass formation and the resulting sample thickness is limited to less than about 50 μm [2]. As exceptional examples, one can observe that Pd–Ni–P and Pt–Ni–P amorphous alloys have lower critical cooling rates of the order of 10^3 K/s [3] and a large amorphous alloy sphere with a diameter of about 10 mm is produced by repeated melting of the Pd–Ni–P alloy covered with a B_2O_3 flux medium in a quartz crucible [4,5]. More recently, since 1988, we have succeeded in finding new multicomponent alloy systems with much lower critical cooling rates in the Mg- [6], Ln- [7], Zr- [8,9], Fe- [10,11], Pd–Cu- [12], Pd–Fe- [13], Ti- [14,15] and Ni-based [16] alloy systems. Figure 1 shows the relationship between the critical cooling rate (R_c), maximum sample thickness (t_{max}) and reduced glass transition temperature (T_g/T_m) for amorphous alloys reported to date [17–21]. The lowest R_c is as low as 0.10 K/s [22] for the $Pd_{40}Cu_{30}Ni_{10}P_{20}$ alloy and the t_{max} reaches values as large as about 100 mm. It is also noticed that the recent improvement of the glass-forming ability (GFA) reaches 6–7 orders for the critical cooling rate and 3–4 orders for the maximum thickness. There is a clear tendency for GFA to increase with increasing T_g/T_m. Figure 2 shows the relationship between R_c, t_{max} and the temperature interval of a

* The Millennium Special Issue — A Selection of Major Topics in Materials Science and Engineering: Current status and future directions, edited by S. Suresh.

1359-6454/00/$20.00
PII: S1359-6454(99)00300-6

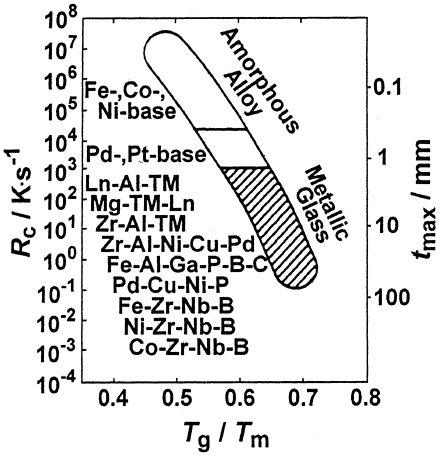

Fig. 1. Relationship between the critical cooling rate for glass formation (R_c), maximum sample thickness for glass formation (t_{max}) and reduced glass transition temperature (T_g/T_m) for bulk amorphous alloys. The data of the ordinary amorphous alloys, which require high cooling rates for glass formation, are also shown for comparison.

Table 1. Bulk amorphous alloy systems and calendar years when details about each alloy system were first published

I. Nonferrous metal base	Years
Mg–Ln–M (Ln = Lanthanide metal, M = Ni, Cu or Zn)	1988
Ln–Al–TM (TM = VI~VIII group transition metal)	1989
Ln–Ga–TM	1989
Zr–Al–TM	1990
Zr–Ti–Al–TM	1990
Ti–Zr–TM	1993
Zr–Ti–TM–Be	1993
Zr–(Nb,Pd)–Al–TM	1995
Pd–Cu–Ni–P	1996
Pd–Ni–Fe–P	1996
Pd–Cu–B–Si	1997
Ti–Ni–Cu–Sn	1998
II. Ferrous group metal base	
Fe–(Al,Ga)–(P,C,B,Si,Ge)	1995
Fe–(Nb,Mo)–(Al,Ga)–(P,B,Si)	1995
Co–(Al,Ga)–(P,B,Si)	1996
Fe–(Zr,Hf,Nb)–B	1996
Co–Fe–(Zr,Hf,Nb)–B	1996
Ni–(Zr,Hf,Nb)–(Cr,Mo)–B	1996
Fe–Co–Ln–B	1998
Fe–(Nb,Cr,Mo)–(P,C,B)	1999
Ni–(Nb,Cr,Mo)–(P,B)	1999

supercooled liquid defined by the difference between glass transition temperature (T_g) and crystallization temperature (T_x), ($T_x - T_g$) [17–21]. One can see a clear tendency for GFA to increase with increasing T_x. The value of T_x exceeds 100 K for several amorphous alloys in Zr–Al–Ni–Cu and Pd–Cu–Ni–P systems and the largest ΔT_x reaches 127 K for the Zr–Al–Ni–Cu base system.

Table 1 summarizes typical bulk amorphous alloy systems reported to date and the calendar years when details of each alloy system were published. Bulk amorphous alloys can be divided into nonferrous and ferrous alloy systems. The nonferrous alloy systems are Mg–Ln–M (Ln = lanthanide metal, M = Ni, Cu or Zn) [23], Ln–Al–TM (TM = VI–VIII group transition metal) [7], Zr–Al–TM [8], Zr–Ti–Al–TM [24,25], Ti–Zr–TM [26], Zr–Ti–TM–Be [9], Zr–(Nb,Pd)–Al–TM [25], Pd–Cu–Ni–P [12], Pd–Fe–Ni–P [13], Ti–Zr–Ni–Cu–Sn [14] and Ti–Zr–Ni–Cu–(Si,B) [15] systems. Ferrous alloy systems comprise Fe–(Al,Ga)–metalloids [10], (Fe,Co,Ni)–(Zr,Hf,Nb)–B [11], Fe–Co–Ln–B [27], Ni–Ti–P [16] and Ni–Nb–(Cr,Mo)–(P,B) [28] alloys. It is observed that the ferrous alloy systems have been found during the last four years after the synthesis of the nonferrous alloy systems. We also examined the features of the alloy components of these nonferrous and ferrous bulk amorphous alloys. The alloy components are divided into five groups, as summarized in Fig. 3. The first group (i) consists of ETM (or Ln), Al and LTM as exemplified for Zr–Al–Ni and Ln–Al–Ni systems. The second group (ii) is composed of LTM, ETM and metalloid as indicated by Fe–Zr–B and Co–Nb–B systems. The third group (iii) is LTM (Fe)–(Al,Ga)–metalloid systems and the fourth group (iv) is indicated by Mg–Ln–LTM and ETM(Zr, Ti)–Be–LTM systems. However, the Pd–Cu–Ni–P and Pd–Ni–P systems (v) are composed only of two kinds of group element (LTM and metalloid), which are different from the combination of the three types of group elements for the alloys belonging to the four previous groups (i)–(iv). Consequently, we must consider two different mechanisms for the achievement of the high stability of the supercooled liquid for the alloys of the first four groups and of the fifth group of alloys.

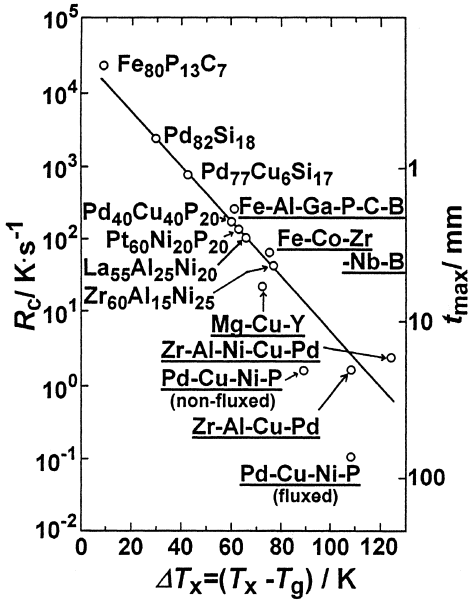

Fig. 2. Relationship between R_c, t_{max} and the temperature interval of the supercooled liquid region between T_g and T_x, ($\Delta T_x = T_x - T_g$) for bulk amorphous alloys.

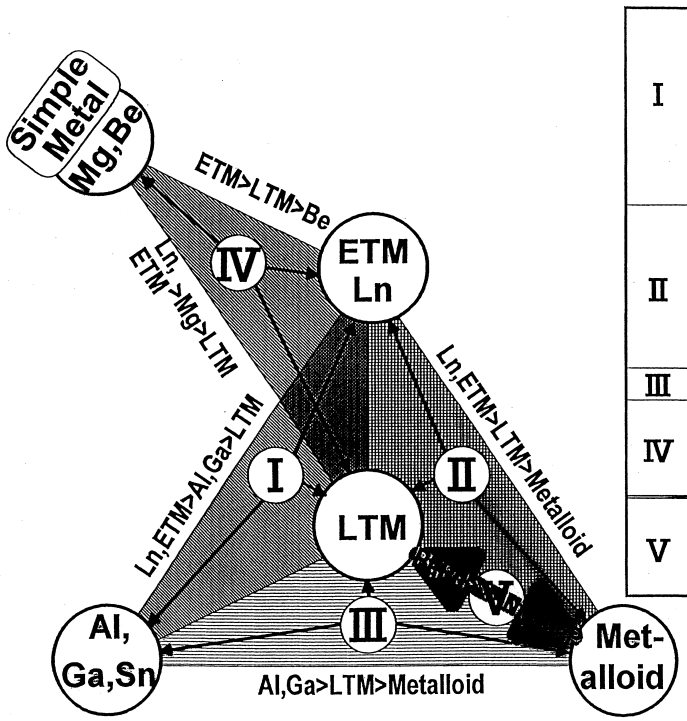

I	Zr-Al-Ni	Ln-Al-Ni
	Zr-Al-Cu	Ln-Al-Cu
	Zr-Al-Ni-Cu	Ln-Al-Ni-Cu
	Zr-Ti-Al-Ni-Cu	Ln-Ga-Ni
	Zr-Nb-Al-Ni-Ln	Ln-Ga-Cu
	Zr-Ga-Ni	
II	Fe-Zr-B	
	Fe-Hf-B	
	Fe-Zr-Hf-B	
	Fe-Co-Ln-B	
	Co-Zr-Nb-B	
III	Fe-(Al,Ga)-metalloid	
IV	Mg-Ln-Ni	
	Mg-Ln-Cu	
	Zr-Ti-Be-Ni-Cu	
V	Pd-Ni-P	
	Pd-Cu-Ni-P	
	Pt-Ni-P	

Fig. 3. Features of alloy components for bulk amorphous alloys reported to date. ETM and LTM represent the transition metals belonging to groups IV–VI and VII–VIII in the periodic table, respectively.

2. STRUCTURE OF BULK AMORPHOUS ALLOYS AND REASONS FOR HIGH GLASS-FORMING ABILITY

Firstly, the reason for the stabilization of the supercooled liquid for the alloys belonging to the groups (i)–(iv) is discussed. All the alloy systems in these groups are based on the following three empirical rules [17–21]: (1) multicomponent systems consisting of more than three elements; (2) significant difference in atomic size ratios above about 12% among the three main constituent elements; and (3) negative heats of mixing among the three main constituent elements. We want to know the reason why the alloys with the three empirical rules can have a high GFA. Based on the previously reported experimental data obtained for multicomponent amorphous alloys, it has been clarified [17–21] that amorphous alloys can have (a) higher degrees of dense randomly packed atomic configurations, (b) new local atomic configurations, which are different from those of the corresponding crystalline phases, and (c) a homogeneous atomic configuration of the multicomponents on a long-range scale. Subsequently, some experimental data are presented. Table 2 summarizes the densities of some bulk amorphous alloys in as-cast and fully crystallized states. The difference in the densities between the as-cast amorphous and fully crystallized states is in the range of 0.30–0.54% [29], which is much smaller than the previously reported value range of about 2% [30] for ordinary amorphous alloys with much higher R_c above 10^5 K/s. Such small differences in values indicate that the bulk amorphous alloys have higher dense randomly packed atomic configurations. Although the difference in densities between the amorphous and crystalline phases is

Table 2. Densities of some bulk amorphous alloys in as-cast and fully crystallized states

Alloy (state)	ρ_{cast} (Mg/m^3) (Amorphous)	$\rho_{relaxed}$ (Mg/m^3) (Amorphous)	ρ_{cryst} (Mg/m^3) (Crystal)	$\Delta\rho_{relaxed}$ (%)[a] –	$\Delta\rho_{cryst}$ (%)[b] –
$Zr_{60}Al_{10}Cu_{30}$	6.72	–	6.74	–	0.30
$Zr_{55}Al_{15}Ni_{25}$	6.36	–	6.38	–	0.31
$Zr_{55}Cu_{30}Al_{10}Ni_5$	6.82	6.83	6.85	0.15	0.44
$Pd_{40}Cu_{30}Ni_{10}P_{20}$	9.27	9.28	9.31	0.11	0.54
$Zr_{55}Ti_5Al_{10}Cu_{20}Ni_{10}$	6.62	–	6.64	–	0.30
$Zr_{52.5}Ti_5Al_{12.5}Cu_{20}Ni_{10}$	6.52	–	6.65	–	0.45

[a] $\Delta\rho_{relaxed} = (\rho_{relaxed} - \rho_{cast})/\rho_{cast.}$.
[b] $\Delta\rho_{cryst} = (\rho_{cryst} - \rho_{cast})/\rho_{cast.}$.

Table 3. Coordination numbers and atomic distances calculated from (a) the ordinary radial distribution function (RDF), and from the environmental RDFs for (b) Zr and (c) Ni in the $Zr_{60}Al_{15}Ni_{25}$ amorphous alloy

Alloy		r_1 (nm)	N_{ZrNi}	r_2 (nm)	N_{ZrAl}	N_{ZrAl}
As-quenched	(a)	0.267 ± 0.002	2.3 ± 0.2	0.317 ± 0.002	10.3 ± 0.7	-0.1 ± 0.9
	(b)	0.267 ± 0.002	2.1 ± 0.2	–	–	–
	(c)	0.269 ± 0.002	2.3 ± 0.2	–	–	–
Crystallized	(a)	0.268 ± 0.002	3.0 ± 0.2	0.322 ± 0.002	8.2 ± 0.7	0.8 ± 0.9
	(b)	0.267 ± 0.002	3.0 ± 0.2	–	–	–
	(c)	0.273 ± 0.002	2.3 ± 0.2	–	–	–

small, a systematic increase in the density by structural relaxation, followed by a significant increase upon crystallization, has been confirmed for the $Pd_{40}Cu_{30}Ni_{10}P_{20}$ alloy [21]. We further examined the coordination numbers and atomic distances of each atomic pair for the multicomponent bulk amorphous alloys by the anomalous X-ray scattering technique and always noticed the existence of at least one atomic pair with significant difference in coordination numbers before and after crystallization. For instance, Table 3 summarizes the coordination numbers and atomic distances calculated from (a) the ordinary radial distribution function (RDF), and from the environmental RDFs for (b) Zr and (c) Ni in the $Zr_{60}Al_{15}Ni_{25}$ amorphous alloy [31]. As compared with the changes in the coordination numbers and atomic distances of Zr–Ni and Zr–Zr atomic pairs, the coordination number of the Zr–Al atomic pair increases drastically after crystallization. The significant change implies the necessity of long-range atomic rearrangements of Al atoms around Zr for the progress of crystallization as well as the difference in the local atomic configurations between the amorphous and crystalline phases. Furthermore, neither splitting of the second peak nor pre-peak at the lower wave vector is seen in the total structure factors of the multicomponent amorphous alloys. This feature of the structure factors is nearly the same as that found for ordinary alloy liquids, indicating the homogeneous distribution of constituent elements on a long-range scale. As summarized in Table 4, in a new type of supercooled liquid with a higher degree of dense randomly packed atomic configurations, new local atomic configurations and long-range homogeneous atomic configurations, we have high solid/liquid interfacial energy which is favorable for the suppression of nucleation of a crystalline phase. The new type of liquid can have the difficulty of atomic rearrangement, leading to a decrease of atomic diffusivity

Table 4. Mechanisms for the stabilization of supercooled liquid and the high glass-forming ability for the multicomponent alloys which satisfy the three empirical rules

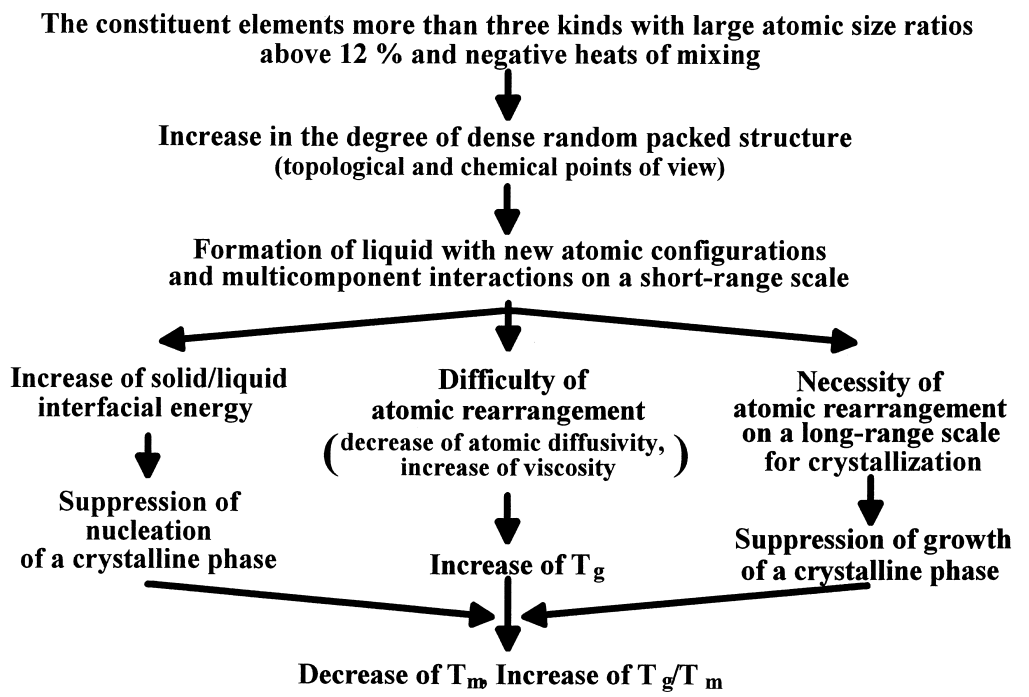

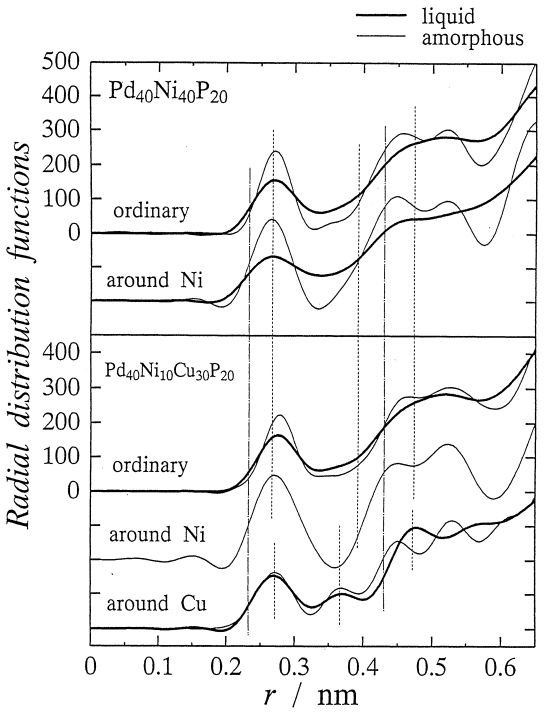

Fig. 4. Ordinary radial distribution function (RDF) and environmental RDFs around Ni and Cu atoms for a $Pd_{40}Cu_{30}Ni_{10}P_{20}$ amorphous alloy.

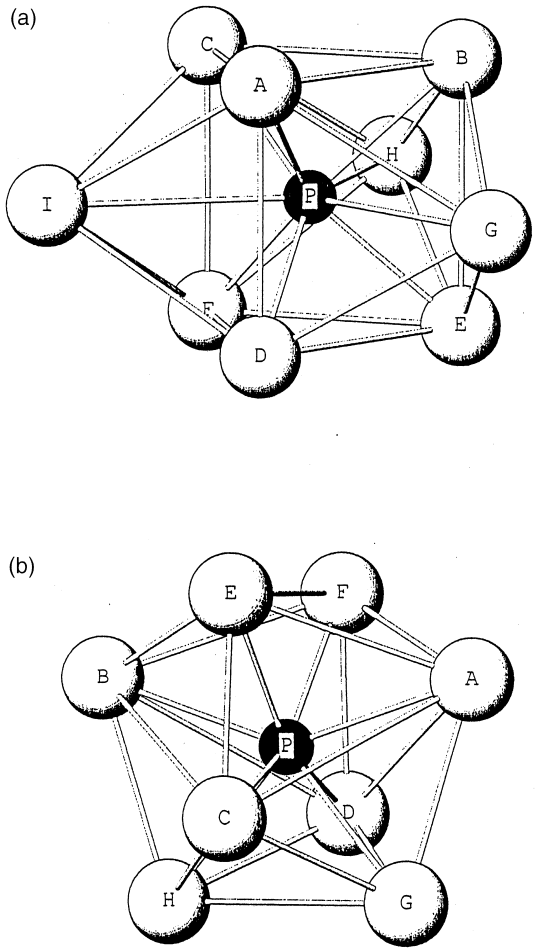

Fig. 5. Schematic illustration of a trigonal prism capped with three half-octahedra consisting of Pd, Ni and P atoms and a tetragonal dodecahedron consisting of Pd, Cu and P atoms.

and an increase of viscosity. Therefore, the new liquid can have high T_g. The supercooled liquid also has the necessity for atomic rearrangements on a long-range scale for crystallization, which causes the suppression of growth of a crystalline phase. In any event, the multicomponent alloys with the three empirical rules always have very deep eutectic valleys with low melting temperatures, leading to the appearance of high T_g/T_m and large ΔT_x. Therefore, a high thermal stability of supercooled liquid for the multicomponent amorphous alloys which satisfies the three empirical rules is observed.

As shown in Fig. 3, the Pd–Cu–Ni–P and Pd–Ni–P amorphous alloys do not satisfy the three empirical rules because the heats of mixing are nearly zero for Pd–Cu and Pd–Ni pairs [32] and the atomic size ratios between Pd and Cu or Ni is less than 10% [33]. In order to investigate the origin of the achievement of high stability of supercooled liquid against crystallization, we examined the structure of the $Pd_{40}Cu_{30}Ni_{10}P_{20}$ amorphous alloy by the anomalous X-ray scattering method. Figure 4 shows the ordinary radial distribution function and environmental radial distribution functions around Ni and Cu atoms for the Pd–Cu–Ni–P amorphous alloy [34], together with the data for the $Pd_{40}Ni_{40}P_{20}$ amorphous alloy. The environmental RDF around Ni for the Pd–Cu–Ni–P alloy is nearly the same as that for the Pd–Ni–P alloy, while the partial RDF around the Cu atom is different from that around the Ni atom, indicating that the local atomic configuration around Cu is different from that around Ni. The atomic distances and coordination numbers of each atomic pair obtained from the structural data for the Pd–Cu–Ni–P alloy can be interpreted by the assumption that the Pd–Cu–Ni–P amorphous alloy is composed of two large clustered units of a trigonal prism capped with three half-octahedra for the Pd–Ni–P region and a tetragonal dodecahedron for the Pd–Cu–P region, as illustrated in Fig. 5. The coexistence of the two large clustered units seems to play an important role in the stabilization of the supercooled liquid for the Pd-based alloy, because of the strong bonding nature of metal–metalloid atomic pairs in the clustered units, high stability of metal–metalloid clustered units and difficulty of rearrangement among the clustered units. Furthermore, the GFA of the Pd–Cu–Ni–P alloy is much higher than that for the Pd–Ni–P alloy and the difference is due to the coexistence of the two large clustered units of the trigonal prism and tetragonal dodecahedron rather than the existence of only the trigonal prism.

3. PRODUCTION OF BULK AMORPHOUS ALLOYS

By choosing the above-described multicomponent alloy systems, we can produce bulk amorphous alloys by using two kinds of production techniques of solidification and consolidation [17–21]. As a solidification technique, one can list water-quenching, copper-mold casting, high-pressure die casting, arc melting, unidirectional melting, suction casting and squeeze casting. Bulk amorphous alloys are also produced by hot pressing and warm extrusion of atomized amorphous powders in the supercooled liquid region. Table 5 summarizes t_{max} by use of the solidification techniques and approximates R_c in typical alloy systems. The value of t_{max} is about 10 mm for the Ln- [35] and Mg-based [36] alloys, 30 mm [37] for the Zr-based alloys, 5–6 mm for the Fe- [38] and Ti-based [14] alloys, 75–80 mm [39] for the Pd–Cu–Ni–P alloy and 3 mm [28] for the Ni-based alloy. There is a clear tendency for t_{max} to increase with decreasing R_c. As examples, Fig. 6 shows the shape and outer surface appearance of typical bulk amorphous alloys 17 mm in diameter and 600 or 120 mm in length for the $Zr_{60}Al_{10}Ni_{10}Cu_{20}$ amorphous alloy and 75 mm in diameter and 80 mm in height for the $Pd_{40}Cu_{30}Ni_{10}P_{20}$ amorphous alloy. These bulk amorphous alloys have smooth outer surfaces and good metallic luster. By using these bulk amorphous alloys, R_c is determined accurately through the construction of continuous cooling transformation (CCT) curve. Figure 7 shows the CCT curves of the $Pd_{40}Cu_{30}Ni_{10}P_{20}$ alloy in the non-fluxed and B_2O_3 fluxed states [22]. The R_c value is 1.58 K/s in the non-fluxed state and decreases to 0.100 K/s in the fluxed state. The B_2O_3 flux treatment is useful to decrease the R_c value because of the decrease in heterogeneous nucleation of crystalline phases through the purification of the molten alloy [29,30]. In order to confirm further the importance of the suppression of heterogeneous nucleation, we evaluated the temperature–time-transformation (TTT) curve under the assumption of the absence of heterogeneous nucleation. The calculated R_c value decreases further by two orders to 0.001 K/s. This result indicates that the heterogeneous nucleation cannot be completely eliminated even by the B_2O_3 flux treatment.

Table 5. Maximum thickness (t_{max}) and critical cooling rate (R_c) of bulk metallic glasses

Alloy system	t_{max} (mm)	R_c(K/s)
Ln–Al–(Cu,Ni)	≅10	≅200
Mg–Al–(Cu,Ni)	≅10	≅200
Zr–Al–(Cu,Ni)	≅30	1–10
Zr–Ti–Al–(Cu,Ni)	≅30	1–5
Zr–Ti–(Cu,Ni)–Be	≅30	1–5
Fe–(Al,Ga)–(P,C,B,Si)	≅3	≅400
Pd–Cu–Ni–P	≅75	0.1
Fe–(Co,Ni)–(Zr,Hf,Nb)–B	≅6	≅200
Ti–Ni–Cu–Sn	≅6	≅200

4. MECHANICAL PROPERTIES

In addition to the importance of basic science, it is important in applications as engineering materials to clarify the mechanical properties of bulk amorphous alloys. Figure 8 shows the relationship between the tensile fracture strength (σ_f) and Young's modulus (E) for the cast bulk amorphous Zr–Ti–Al–Ni–Cu alloys in sheet and cylinder forms with thicknesses (or diameters) of 1–5 mm [21]. There is a clear tendency for σ_f to increase with increasing E. Figure 9 shows the relationship between σ_f or H_v and E for bulk amorphous Mg–Cu–Y, La–Al–Ni, La–Al–Co–Ni–Cu, Zr–Ti–Al–Ni–Cu, Pd–Cu–Ni–P and Ti–Zr–Ni–Cu–Sn alloys together with the data of conventional crystalline alloys. The bulk amorphous alloys have high σ_f of 840–2100 MPa combined with E of 47–102 GPa which depend on alloy compositions. The bulk amorphous alloys exhibit higher σ_f, higher H_v and lower E than those of any kinds of crystalline alloys. The feature of the mechanical properties for the bulk amorphous alloys is significantly different from that for the crystalline alloys. We further examined the compositional dependence of Charpy impact fracture energy for the cast bulk amorphous $Zr_{70-x-y}Ti_xAl_yCu_{20}Ni_{10}$ sheets with a thickness of 2.5 mm [40]. The impact fracture energy is in the range of 122–135 kJ/m^2 for the Zr-based alloys containing 0–5 at.% Ti and 10 at.% Al and tends to decrease with the deviation from the alloy composition range. We also measured the three-point bending flexural stress and deflection curves of the Zr–Al–Ni–Cu and Zr–Ti–Al–Ni–Cu bulk amorphous alloys [40]. These bulk amorphous alloys have high bending flexural strength values of 3000–3900 MPa which are 2.0–2.5 times higher than those for crystalline Zr- and Ti-based alloys. Furthermore, all these bulk amorphous alloys have large deflection values above 0.4 mm. Figure 10 summarizes the bending and rotating beam fatigue strength as a function of number up to failure for the bulk amorphous $Zr_{65}Al_{10}Ni_{10}Cu_{15}$ [21] and $Pd_{40}Cu_{30}Ni_{10}P_{20}$ [41] alloys, respectively, together with the data under tensile stress conditions for melt-spun $Pd_{80}Si_{20}$ [42], $Ni_{75}Si_8B_{17}$ [43] and $Co_{75}Si_{10}B_{15}$ [43] amorphous ribbons. When the fatigue limit is defined by the ratio of the minimum fatigue strength after 10^7 cycles to the static bending or tensile fracture strength, the fatigue limit of the bulk amorphous alloys is in the range of 0.20–0.30, in agreement with the previous results [42,43] for the melt-spun amorphous ribbons. The bending fatigue strength is as high as about 1000 MPa at cycles of 3×10^4. It is thus confirmed that the present Zr- and Pd–Cu-based bulk amorphous alloys have good combination of various mechanical prop-

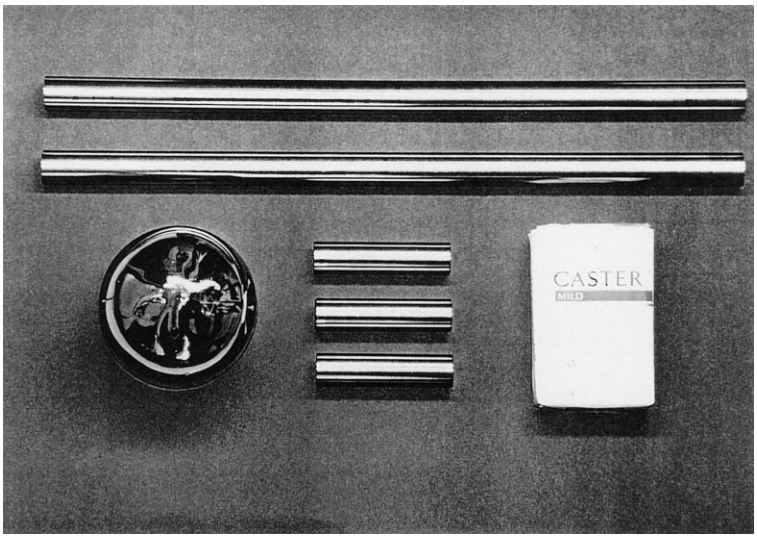

Fig. 6. Outer surface morphology of bulk amorphous alloys. The cylindrical ingot of 75 mm in diameter and 80 mm in height and the cylindrical bar of 17 mm in diameter and 600 or 120 mm in length are composed of $Pd_{40}Cu_{30}Ni_{10}P_{20}$ and $Zr_{60}Al_{10}Ni_{10}Cu_{20}$ alloys, respectively.

erties, which cannot be obtained for conventional crystalline alloys.

In addition to the high Charpy impact fracture energy, high fatigue strength, large bending deflection and large elastic elongation, it is important to clarify the fracture toughness and fracture mechanics of bulk amorphous alloys for the extension of application fields of bulk amorphous alloys as high-strength materials. There is a high possibility that bulk amorphous alloys contain some flaws. We want to know the maximum stress that the bulk amorphous alloy can withstand if it contains flaws of a certain size and geometry. Fracture toughness represents the ability of the amorphous alloy containing a flaw to withstand an applied load. As compared with the results of an impact test, fracture toughness is a quantitative property of the alloy. The shape and dimension of the test specimens used for the measurement of fracture toughness of a $Zr_{55}Al_{10}Ni_5Cu_{30}$ bulk amorphous alloy agree with ASTM criteria. Assuming that the stress field near the crack tip is controlled by linear fracture mechanics and the small-scale yielding condition, the fracture toughness (K-value) can be evaluated according to ASTM criteria. The measured K_c values of Zr-based amorphous alloys with a thickness of 3 mm are about 67 $MPa\sqrt{m}$ for $Zr_{55}Al_{10}Ni_5Cu_{30}$ and 70 $MPa\sqrt{m}$ for $Zr_{55}Al_{10}Ni_5Cu_{29}Nb_1$ [21]. In the fracture surface region near the crack tip shown in Fig. 11, a vein fracture pattern is observed and no appreciable embrittled pattern is seen, indicating that these bulk amorphous alloys have high plastic deformability

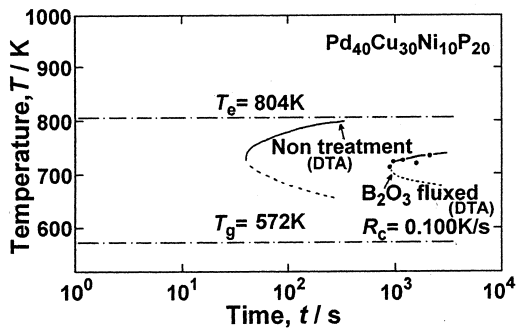

Fig. 7. Continuous cooling curves in the unfluxed and fluxed states for a $Pd_{40}Cu_{30}Ni_{10}P_{20}$ alloy liquid.

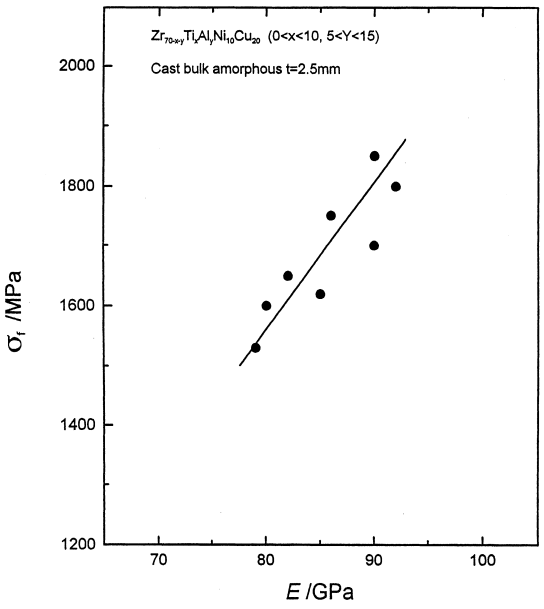

Fig. 8. Relationship between tensile fracture strength (σ_f) and Young's modulus (E) for bulk amorphous $Zr_{70-x-y}Ti_xAl_yNi_{10}Cu_{20}$ alloy sheets.

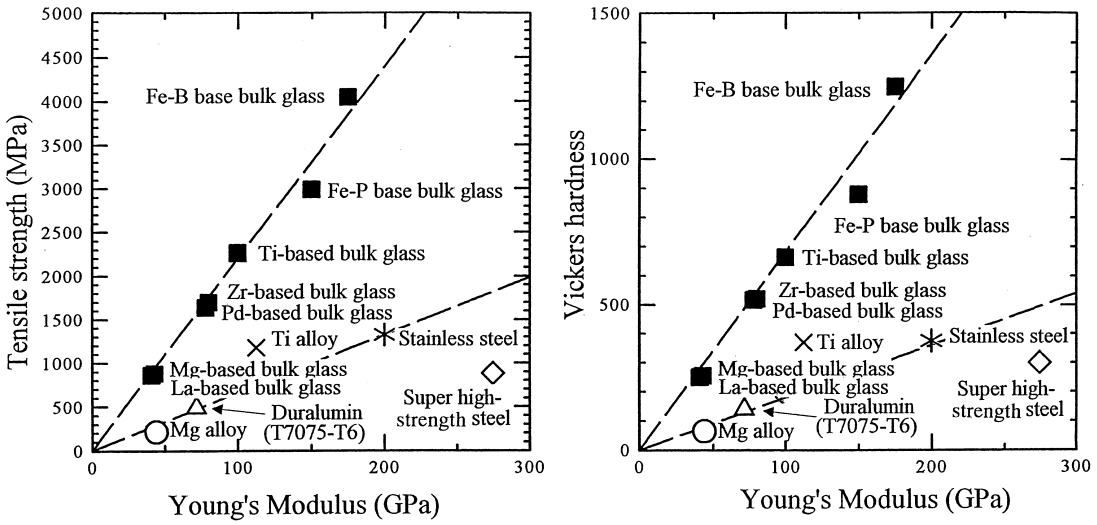

Fig. 9. Relationship between σ_f or Vickers hardness (H_v) and E for various bulk amorphous alloys.

even near the pre-existent crack tip. These data were obtained for the sheet specimen with a thickness of 3.0 mm. It is not certain whether or not the K values correspond to the plain strain fracture toughness (K_{Ic}). However, it is noticed that the K values are much higher than those (24–36 MPa$\sqrt{m}$) [44] for age-hardened Al-based alloys and comparable to those (54–98 MPa$\sqrt{m}$) [44] for commercial Ti-based alloys. The K values are also higher than that (55 MPa$\sqrt{m}$) [45] for the Zr–Ti–Be–Ni–Cu bulk amorphous alloy. Here, it is particularly important to point out that the K values decrease to about 1 MPa$\sqrt{m}$ for the Zr–Ti–Be–Ni–Cu amorphous alloy containing nanocrystalline particles [46], while the Zr–Al–Ni–Cu base bulk amorphous alloys containing nanocrystalline particles exhibit a remarkably improved K value of about 160 MPa$\sqrt{m}$ [47], which exceeds largely those of conventional Ti- and alloy steels. For the measurement of a real K value for the bulk amorphous alloy containing nanocrystalline particles with high fracture toughness, it is necessary to use bulk amorphous alloys with much larger thicknesses.

5. CORROSION RESISTANCE

When bulk amorphous alloys for their good static and dynamic mechanical properties are used as structural materials, it is essential for the bulk amorphous alloys to have good corrosion resistance in various kinds of corrosive solutions. There have been no data published on the corrosion resistance of Zr-based bulk amorphous alloys in any kinds of corrosive solution. We examined the corrosion resistance of melt-spun amorphous alloys in Zr–TM–Al–Ni–Cu (TM = Ti,Cr,Nb,Ta) systems in HCl and NaCl solutions and noticed that the Nb- and Ta-containing amorphous alloys exhibit good corrosion resistance in their solutions at room temperature [21, 48]. We have confirmed that the X-ray diffraction patterns of melt-spun $Zr_{60-x}M_xAl_{10}Ni_{10}Cu_{20}$ (M = Ti,Nb,Ta; x = 5–20 at.%) alloys consist only of a main broad peak at a wave vector K_p of 26–27 nm^{-1} and no appreciable diffraction peak due to the precipitation of a crystalline phase is seen over the composition range up to 20 at.% of Ti, Nb or Ta. However, the formation of $Zr_{60-x}Cr_xAl_{10}Ni_{10}Cu_{20}$ amorphous alloys was limited to less than 10 at.%Cr. Figure 12 shows the corrosion rates of the $Zr_{60-x}TM_xAl_{10}Ni_{10}Cu_{20}$ (TM = Ti,Cr,Nb,Ta) amorphous alloys subjected to immersion for 16 and 64 h in 6M HCl solution at 295 K. The corrosion rates of the Zr–Al–Ni–Cu and Zr–Cr–Al–Ni–Cu amorphous alloys are too high to measure after immersion for 64 h, even though the corrosion rates of their amorphous alloys in 1 M HCl show very low values below 0.01 mm/year. Even in severe corrosive solution, the Nb- and Ta-containing alloys exhibit rather low corrosion rates below 0.1 mm/year after immersion for 64 h. Figure 12 also shows that the effect of the additional elements on the corrosion resistance is largest for Nb, followed by Ta, Ti and then Cr.

It is also important to clarify the corrosion resistance of the Zr-based amorphous alloys in NaCl solution. Figure 13 shows the current density as a function of potential in 3 mol% NaCl solution at 298 K for $Zr_{60}Al_{10}Ni_{10}Cu_{20}$, $Zr_{55}Ti_{2.5}Al_{12.5}Ni_{10}Cu_{20}$ and $Zr_{55}Nb_5Al_{10}Ni_{10}Cu_{20}$ amorphous alloys, together with the data of pure crystalline Zr metal. The solution was exposed in air. The corrosion resistance is largest for the Nb-containing alloy, followed by the Ti-containing alloy and then the Zr–Al–Ni–Cu alloy. The corrosion resistance of the Nb-containing alloy is also superior to that for pure Zr metal, indicating the remarkable effectiveness of

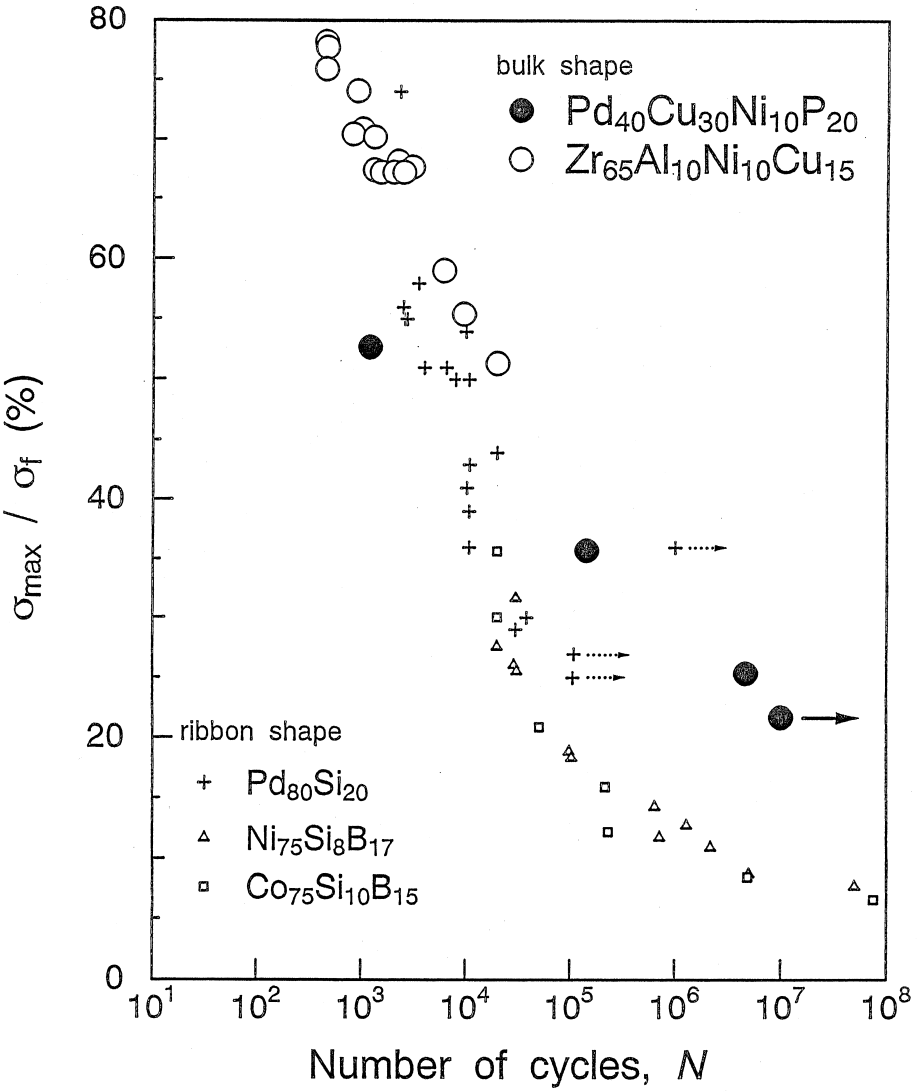

Fig. 10. Maximum bending and rotating beam fatigue stress as a function of cyclic number up to failure for bulk amorphous $Zr_{65}Al_{10}Ni_{10}Cu_{15}$ and $Pd_{40}Cu_{30}Ni_{10}P_{20}$ alloys. The data under tensile stress conditions for melt-spun Pd-, Ni- and Co-based amorphous ribbons are also shown for comparison.

Nb addition on the improvement of corrosion resistance even in the NaCl solution. Considering the previous data [25] that a bulk amorphous $Zr_{55}Nb_5Al_{10}Ni_{10}Cu_{20}$ ingot with a thickness of 8 mm was produced by the simple process of arc melting, followed by cooling on a copper hearth cooled with water, the addition of about 5 at.% Nb is concluded to be useful for the formation of bulk amorphous Zr-based alloys exhibiting good corrosion resistance.

6. HIGH STRAIN-RATE SUPERPLASTICITY

As described above, the bulk amorphous alloys have a wide supercooled liquid region of more than 60 K before crystallization. Figure 14 shows the change in viscosity with reduced temperature ($T_r = T/T_m$) for the $Pd_{40}Cu_{30}Ni_{10}P_{20}$ amorphous alloy [49]. The data of SiO_2 glass are also shown for comparison. The viscosity of the Pd-based amorphous alloy has much larger temperature dependence as compared with SiO_2 glass, indicating that the Pd-based amorphous alloy belongs to the fragile type glass which is different from the strong type of SiO_2 glass. The steep temperature dependence of viscosity causes the low values of 10^5–10^8 Pa·s in the supercooled liquid region. Here, it is important to describe that the low viscosities correspond to very short relaxation times of 10^{-5}–10^{-2} s [3]. By utilizing the short relaxation times, it is expected to have a high strain-rate flowability for the bulk amorphous alloys. Therefore, we examined the deformation behavior in the supercooled liquid region for the bulk amorphous alloys. Figure 15 shows the relation between flow stress and strain rate for the

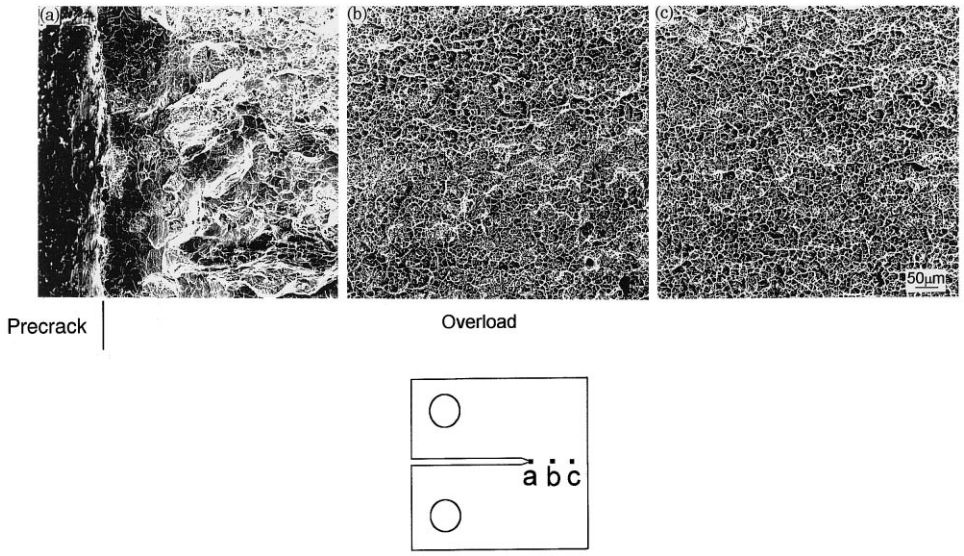

Fig. 11. Fracture surface appearance near the pre-existent crack tip for the bulk amorphous $Zr_{55}Al_{10}Ni_5Cu_{30}$ sheet subjected to fracture toughness measurement. The SEM images (a), (b) and (c) were taken from the regions of a, b and c, respectively, in the illustration.

$Zr_{65}Al_{10}Ni_{10}Cu_{15}$ [50] and $La_{55}Al_{20}Ni_{25}$ [51] amorphous alloys. The T_g is 653 K for the Zr-based alloy and 473 K for the La-based alloy. The flow stress in the supercooled liquid region is proportional to strain rate in the strain-rate range of 10^{-3}–10^{-1} s^{-1} for both alloys, suggesting that the deformation obeys the Newtonian flow behavior in an appropriate strain-rate condition. In order to confirm the achievement of the Newtonian flow, the data in Fig. 15 were analyzed by using the relation $\eta = \sigma/3\dot{\varepsilon}$ [52], where η is viscosity, σ is flow stress and $\dot{\varepsilon}$ is strain rate. The resulting viscosities of the Zr–Al–Ni–Cu and La–Al–Ni amorphous alloys are plotted as a function of strain rate in Fig. 16. The viscosity in the supercooled liquid region is independent of strain rate in a wide strain-rate range up to about 0.1 s^{-1}, indicating the achievement of Newtonian flow in the wide strain-rate range. With further increasing strain rate, the viscosity is dependent on strain rate and decreases almost linearly, indicating that the deformation behavior of the

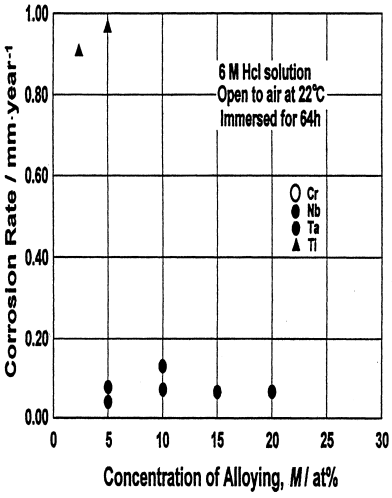

Fig. 12. Corrosion rates of the $Zr_{60-x}TM_xAl_{10}Ni_{10}Cu_{20}$ (TM = Ti, Cr, Nb or Ta) amorphous alloys subjected to immersion for 16 and 64 h in 6 M HCl solution at 295 K.

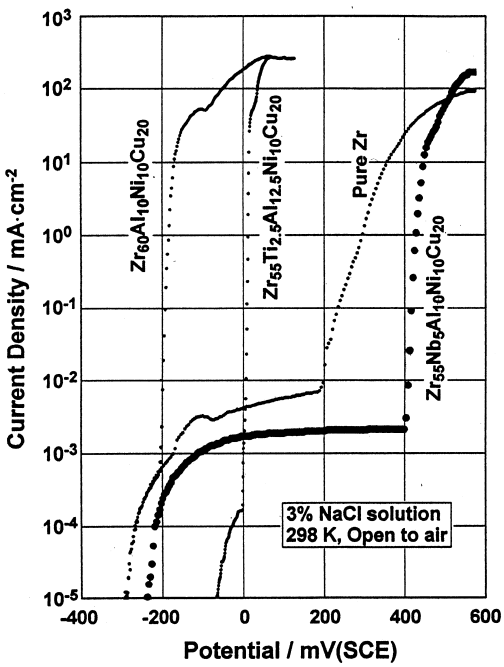

Fig. 13. Current density as a function of potential in 3% NaCl solution at 298 K for $Zr_{60}Al_{10}Ni_{10}Cu_{20}$, $Zr_{55}Ti_{2.5}Al_{12.5}Ni_{10}Cu_{20}$ and $Zr_{55}Nb_5Al_{10}Ni_{10}Cu_{20}$ amorphous alloys, together with the data for pure crystalline Zr metal.

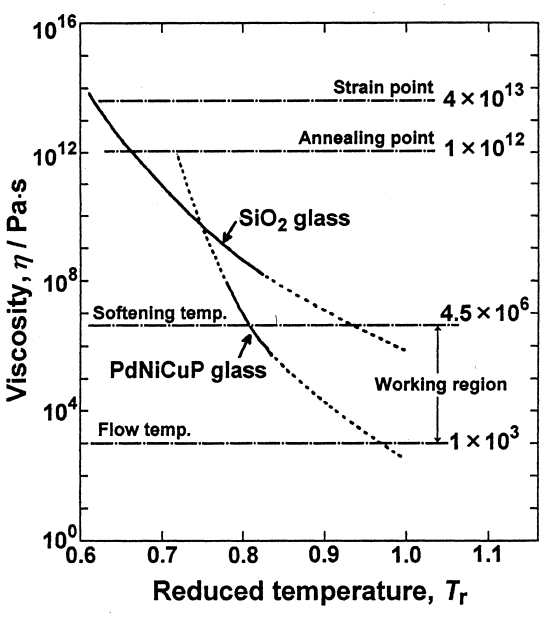

Fig. 14. Viscosity as a function of reduced temperature (T/T_m) for a $Pd_{40}Cu_{30}Ni_{10}P_{20}$ amorphous alloy.

supercooled liquid changes from Newtonian flow to non-Newtonian flow. Furthermore, the deformation mode of the amorphous solid occurs through the non-Newtonian flow and hence it is concluded that the Newtonian flow can occur only in the supercooled liquid region. There is no appreciable difference in the features of non-Newtonian flow mode in the supercooled liquid and amorphous solid. The independence of viscosity with strain rate is important for practical use of viscous flow working in the supercooled liquid region of bulk amorphous alloys. With the aim of clarifying in more detail the Newtonian flow behavior in the supercooled liquid, we examined the relation between true stress (σ) and $\dot{\varepsilon}$ in the supercooled liquid for the $Zr_{55}Al_{10}Ni_5Cu_{30}$ amorphous alloy. A good linear relation is recognized in the relation between σ and $\dot{\varepsilon}$ shown in Fig. 17 and the linear relation is expressed by $\sigma = K\dot{\varepsilon}^m$ [53]. The slope of the linear relation corresponds to the strain-rate sensitivity exponent (m value) and the m value is as large as 1.0, indicating the achievement of ideal Newtonian flow, namely, an ideal superplasticity. A similar Newtonian flow has also been observed for the $Pd_{40}Cu_{30}Ni_{10}P_{20}$ amorphous alloy [54], as recognized that the viscosity is independent of $\dot{\varepsilon}$ while η increases linearly with σ.

We also tried to determine a deformation condition in which a maximum elongation by viscous flow is obtained. Figure 18 shows the relation between elongation at different testing temperatures and strain rates for the $Zr_{65}Al_{10}Ni_{10}Cu_{15}$ and $La_{55}Al_{20}Ni_{25}$ amorphous alloys, together with data for ductility of the deformed samples [50,51]. The maximum elongation is obtained in the supercooled liquid and at a constant deformation condition where the strain rate lies in the Newtonian flow region just below the transition from Newtonian to non-Newtonian flow. The maximum elongation is about 350% for the Zr-based alloy and about 1800% for the La-based alloy with both alloys maintaining good bending ductility when exhibiting maximum elongation. The decrease in elongation in the lower strain-rate region is due to the progress of the incipient-stage reaction for crystallization and that in the higher strain-rate region results from a rapid increase in flow volume generated during flow deformation. It is well known that total elongation is strongly dependent on the original cross-section of the specimens. The La-based amorphous alloys exhibit a large elongation of 1800% even in the melt-spun ribbon form with a thickness of about 20 μm. The elongation is expected to increase significantly when using bulk amorphous alloy with a much larger cross-section. It has been reported that elongation reaches about 15 000% [55] for cylindrical specimens with a diameter of 1.5 mm and about 10^6% [56] for cylindrical specimens with a diameter

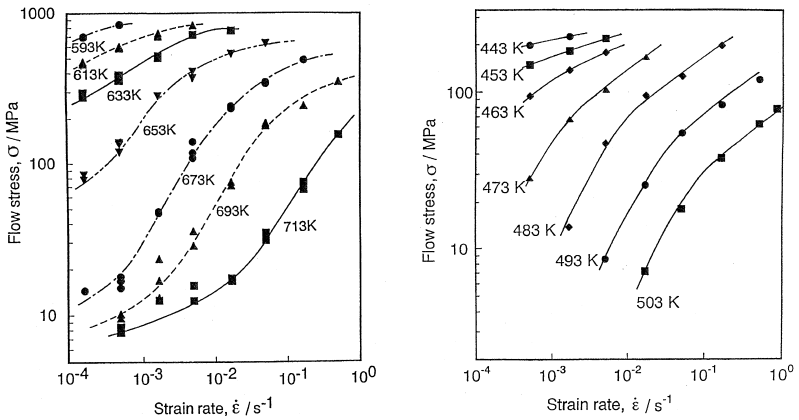

Fig. 15. Relationship between flow stress and strain rate for $Zr_{65}Al_{10}Ni_{10}Cu_{15}$ and $La_{55}Al_{20}Ni_{25}$ amorphous alloys deformed at various temperatures.

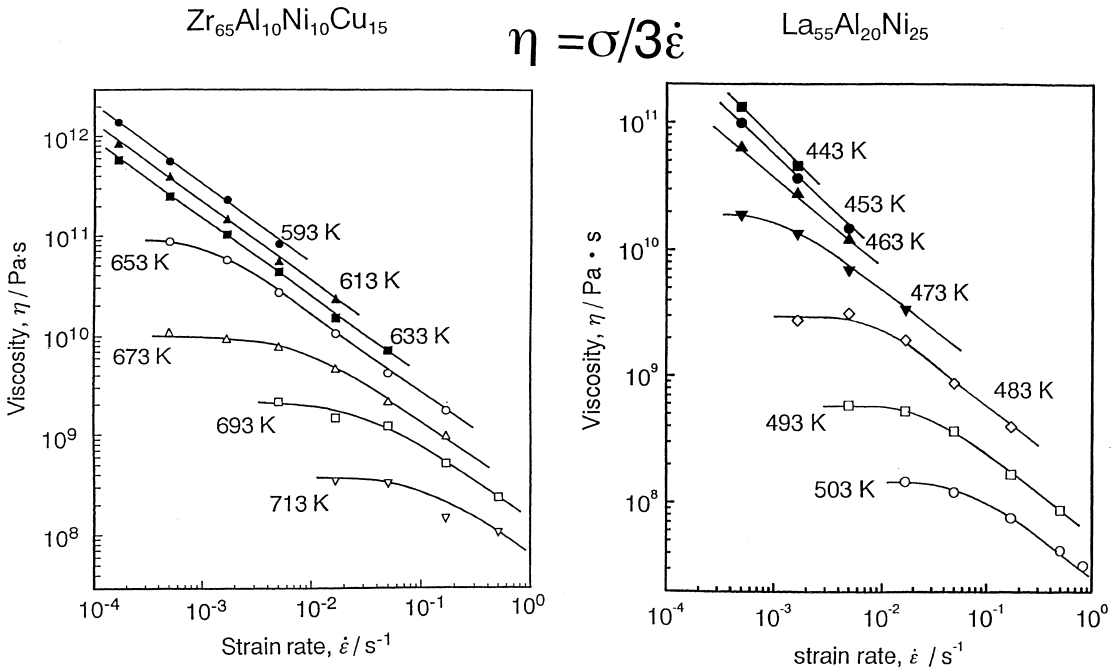

Fig. 16. Viscosity as a function of strain rate for $Zr_{65}Al_{10}Ni_{10}Cu_{15}$ and $La_{55}Al_{20}Ni_{25}$ amorphous alloys deformed at various temperatures.

of 5 mm. Here, it is also important to point out that specimens subjected to heavy tensile deformation also keep good bending ductility. The deformation temperatures and deformation times leading to extremely large elongations were examined in comparison with the isothermal temperature–time-transformation curve of the $La_{55}Al_{20}Ni_{25}$ amorphous alloy. The deformation temperatures and times are located in the higher temperature and longer time region as compared with the onset temperature and time line for crystallization. The distinct discrepancy indicates clearly that the Newtonian-flow deformation in the appropriate deformation condition causes a degradation of crystallization reaction, namely, the deformation-induced stabilization of supercooled liquid. Although the mechanism for the deformation-induced stabilization is not clear, it may be due to the suppression of the incipient reaction for crystallization as well as of the accumulation of flow volumes introduced by the non-Newtonian flow deformation. The finding that the supercooled liquid is stabilized by choosing the Newtonian flow at the appropriate strain rate just below the transition region from Newtonian to non-Newtonian flow is important for further extension of the viscous-flow working of bulk amorphous alloys.

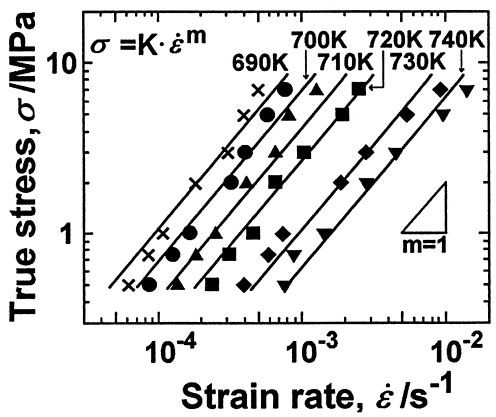

Fig. 17. Relationship between true stress (σ) and strain rate ($\dot{\varepsilon}$) for a $Zr_{65}Al_{10}Ni_5Cu_{30}$ amorphous alloy.

7. MAGNETIC PROPERTIES

Based on the three empirical rules for achievement of high GFA, a new bulk amorphous alloy with ferromagnetism at room temperature has been developed. As described in Section 1, soft ferromagnetic bulk amorphous alloys have been synthesized in multicomponent Fe–(Al,Ga)–(P,C,B,Si) [10], Co–Cr–(Al,Ga)–(P,B,C) [57], Fe–(Co,Ni)–(Zr,Nb,Ta)–B [11] and Co–Fe–(Zr,Nb,Ta)–B [58] systems. This section describes the relationship of soft magnetic properties of new Fe- and Co-based amorphous alloys with high thermal stability of supercooled liquid before crystallization and high GFA in melt-spun ribbon and cast bulk cylinder forms.

7.1. Melt-spun amorphous alloy ribbons

7.1.1. Fe–(Al,Ga)–metalloid systems. Figure 19 shows the *I–H* hysteresis curves of the melt-

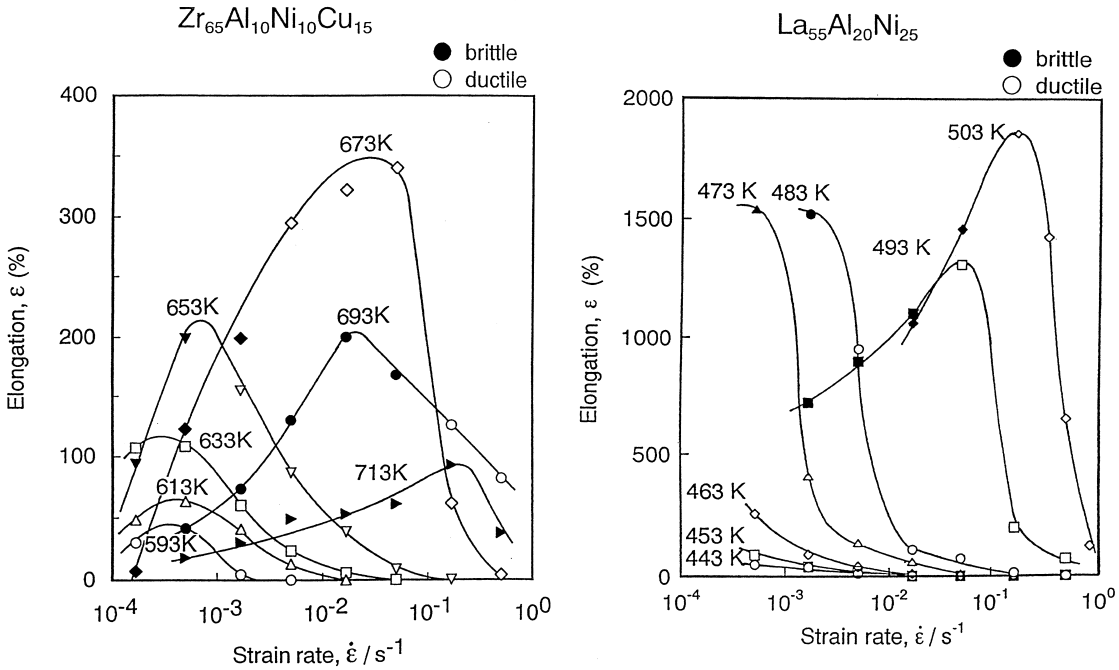

Fig. 18. Relationship between elongation and strain rate for $Zr_{65}Al_{10}Ni_{10}Cu_{15}$ and $La_{55}Al_{20}Ni_{25}$ amorphous alloy ribbons with a thickness of about 20 μm deformed at various temperatures.

spun $Fe_{80}P_{12}B_4Si_4$, $Fe_{76}Al_4P_{12}B_4Si_4$ and $Fe_{74}Al_4Ga_2P_{12}B_4Si_4$ amorphous alloys in an optimally annealed state [59]. It is seen that these amorphous alloys exhibit typical soft magnetic-type hysteresis curves. Table 6 summarizes the magnetic properties of saturation magnetization (I_s), residual magnetization (I_r), squareness ratio (I_r/I_s), coercive force (H_c), effective permeability (μ_e) at 1 kHz and saturated magnetostriction (λ_s) of the three kinds of amorphous alloy ribbons, together with the data of T_g, T_m and T_x. The I_s, H_c and μ_e values, which are important for a soft magnetic material, are about 1.1 T, 5–10 A/m and 12 000 to 19 000, respectively, indicating that the present Fe-based amorphous ribbons possess good soft magnetic properties. In particular, H_c and μ_e are superior to those [60,61] for conventional Fe–Si–B amorphous ribbons, though I_s decreases slightly owing to the lower Fe concentrations. In comparison with those for the Fe–Si–B alloys, the lower H_c and higher μ_e values are presumably due to the lower λ_s value.

In addition to Fe–(Al,Ga)–(P,B,Si) systems, Fe–(Al,Ga)–(P,C,B) [10] and Fe–(Al,Ga)–(P,C,B,Si) [62] amorphous alloys exhibit good soft magnetic properties. Although T_c of the Fe–Al–Ga–P–C–B–Si amorphous alloys decreases monotonously with the replacement of Fe by Si, the other replacement mode, i.e. the replacement of P, Al or C by Si, causes an increase of T_c and the highest T_c for the Fe-based amorphous alloys with ΔT_x above 50 K is 602 K for the $Fe_{72}Al_4Ga_2P_{11}C_6B_4Si_1$ alloy. From the *I–H* hysteresis curves of the $Fe_{72}Al_5Ga_2P_{10}C_6B_4Si_1$, $Fe_{72}Al_4Ga_2P_{11}C_6B_4Si_1$ and $Fe_{72}Al_5Ga_2P_{11}C_5B_4Si_1$ alloys with maximum ΔT_x, it has been confirmed that these amorphous alloys exhibit good soft magnetic properties with 1.06–1.10 T for I_s and 1.03–4.47 A/m for H_c. Figure 20 shows both I_s and H_c as a function of Si content for the four alloy series $Fe_{72-x}Al_5Ga_2P_{11}C_6B_4Si_x$, $Fe_{72}Al_5Ga_2P_{11-x}C_6B_4Si_x$, $Fe_{72}Al_{5-x}Ga_2P_{11}C_6B_4Si_x$

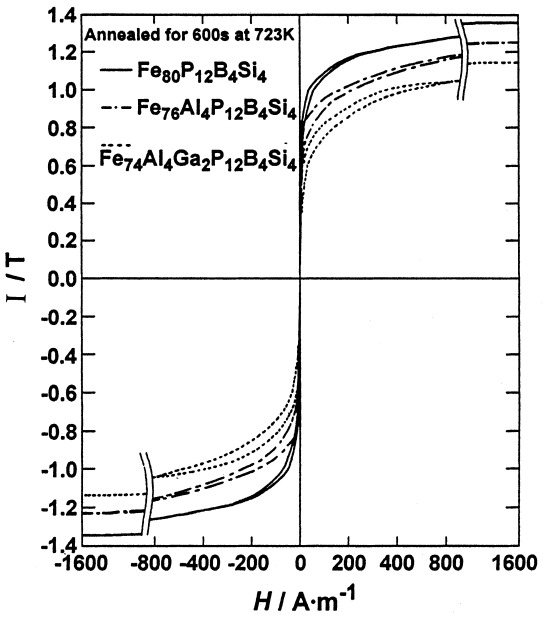

Fig. 19. Hysteresis *I–H* curves of amorphous $Fe_{80}P_{12}B_4Si_4$, $Fe_{76}Al_4P_{12}B_4Si_4$ and $Fe_{74}Al_4Ga_2P_{12}B_4Si_4$ alloys annealed for 600 s at 723 K.

Table 6. Thermal stability and magnetic properties of the amorphous (a) $Fe_{80}P_{12}B_4Si_4$, (b) $Fe_{76}Al_4P_{12}B_4Si_4$ and (c) $Fe_{74}Al_4Ga_2P_{12}B_4Si_4$ alloys

As-quenched									
Alloy	μ_e	H_c (A/m)	I_s (T)	I_r (T)	I_r/I_s	λ_s	T_g (K)	T_x (K)	ΔT_x (K)
(a)	5800	1.3	1.10	0.32	0.29	31×10^{-6}	753	789	36
(b)	2600	12.7	0.96	0.30	0.31	30×10^{-6}	738	780	46
(c)	1900	19.1	0.91	0.27	0.30	21×10^{-6}	737	786	49
Annealed for 600 s at 723 K									
(a)	22 000	1.1	1.34	0.46	0.34				
(b)	21 000	2.6	1.24	0.43	0.35				
(c)	19 000	6.4	1.14	0.40	0.35				

and $Fe_{72}Al_5Ga_2P_{11}C_{6-x}B_4Si_x$. One can see distinct Si dependence of I_s and H_c values. The I_s values increase from 1.04 to 1.13 T with increasing Si content for the latter three alloys where the metalloids are replaced by Si, whereas the replacement of Fe by Si decreases linearly I_s values from 1.04 to 0.665 T. On the other hand, H_c values tend to increase in the range 1.93–18.2 A/m with increasing Si content for the four alloy series. From the compositional dependence of T_x, T_c, I_s and H_c, it is concluded that the $Fe_{72}Al_5Ga_2P_{10}C_6B_4Si_1$ and $Fe_{72}Al_5Ga_2P_{11}C_5B_4Si_1$ amorphous alloys have a good combination of higher thermal stability of supercooled liquid and better soft magnetic properties with higher T_c.

7.1.2. Fe–TM–B systems. The I_s values of melt-spun $Fe_{63-x}Co_xNi_7Zr_{10}B_{20}$ (x = 3, 7, 14 and 17 at.%) amorphous alloys [11] are in the range of 0.91–0.96 T and independent of Co content. On the other hand, the H_c values increase from 2.7 to 10 A/m with increasing Co content from 3 to 17 at.%. The squareness ratio defined by the ratio of I_r to I_s is in the range of 0.32–0.45. From the thermomagnetic data, T_c was measured to be 567 K for the $Fe_{56}Co_7Ni_7Zr_{10}B_{20}$ alloy. These soft magnetic properties were improved by annealing for 600 s at 750 K, which is lower by about 60 K than T_g. That is, I_s, H_c and I_r/I_s of the annealed amorphous alloy are 0.96 T, 2.41 A/m and 0.60, respectively. Furthermore, μ_e at 1 kHz was measured to be 5100 for the as-spun sample and 17 700 for the annealed sample. These magnetic data indicate that the Fe-based amorphous alloy has good soft magnetic properties comparable to those [60,61] for the other Fe-based amorphous alloys, though the I_s value is slightly lower because of the lower Fe concentration.

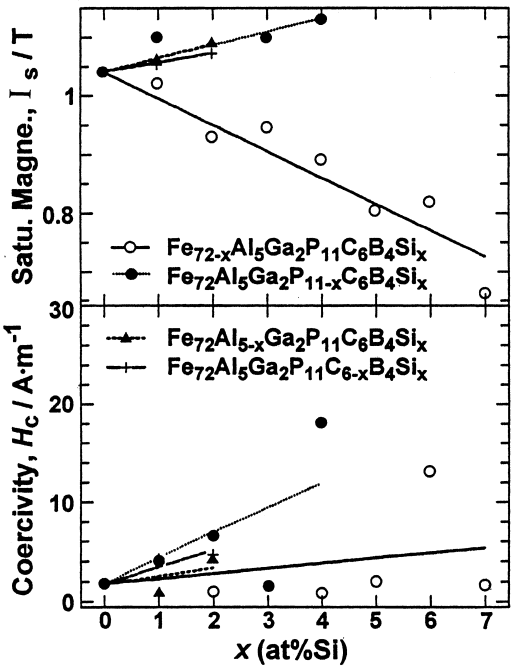

Fig. 20. I_s and H_c as a function of Si content for the amorphous $Fe_{72-x}Al_5Ga_2P_{11}C_6B_4Si_x$, $Fe_{72}Al_5Ga_2P_{11-x}C_6B_4Si_x$, $Fe_{72}Al_{5-x}Ga_2P_{11}C_6B_4Si_x$ and $Fe_{72}Al_5Ga_2P_{11}C_{6-x}B_4Si_x$ alloys.

We measured hysteresis I–H curves of $Fe_{56}Co_7Ni_7Zr_{10-x}Nb_xB_{20}$ amorphous alloys annealed for 300 s at 800 K just below T_g [63]. It has been reported that the replacement of Zr by Nb decreases I_s from 0.96 T at 0 at.% Nb to 0.61 T at 10 at.% Nb through 0.75 T at 2 at.% Nb, while H_c shows low values of 1.1–2.0 A/m and does not have appreciable compositional dependence. Although the total content of Fe and Co elements remains constant, I_s decreases by 0.21 T only by the addition of 2 at.% Nb. The change in I_s with Nb content seems to reflect the change of T_c. The hysteresis I–H curves for the $Fe_{56}Co_7Ni_7Zr_{10-x}Ta_xB_{20}$ amorphous alloys showed a similar change with Ta content [64]. The I_s values decrease gradually from 0.96 to 0.71 T in the range of up to 6 at.% Ta and increases to 0.85 T at 8 at.% Ta, while H_c maintains low values of 2.0–2.7 A/m in the whole Ta content range. Figure 21 shows the changes in μ_e at 1 kHz and λ_s as a function of Nb or Ta content for the $Fe_{56}Co_7Ni_7Zr_{10-x}M_xB_{20}$ (M = Nb or Ta) amorphous alloys in as-spun and annealed (300 s, 800 K) states [63–65], together with the data for I_s and H_c. It is seen that H_c and μ_e are significantly improved by the annealing treatment, though no distinct changes in I_s and λ_s are recognized. The maximum μ_e for the annealed samples reaches 25 000 at 2 at.% Nb and 16 700 at 8 at.% Ta. The compositions showing maximum μ_e values agree with

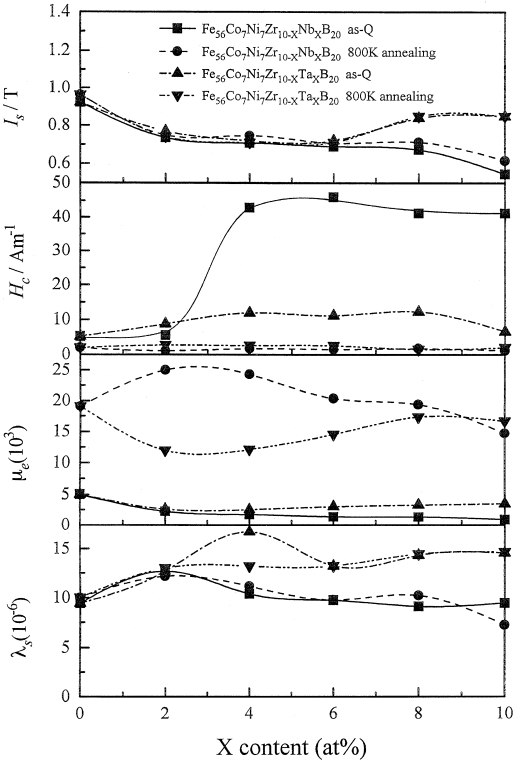

Fig. 21. I_s, H_c, μ_e at 1 kHz and λ_s as a function of Nb or Ta content for the amorphous $Fe_{56}Co_7Ni_7Zr_{10-x}Nb_xB_{20}$ and $Fe_{56}Co_7Ni_7Zr_{10-x}Ta_xB_{20}$ alloys in the as-quenched and annealed (300 s, 800 K) states.

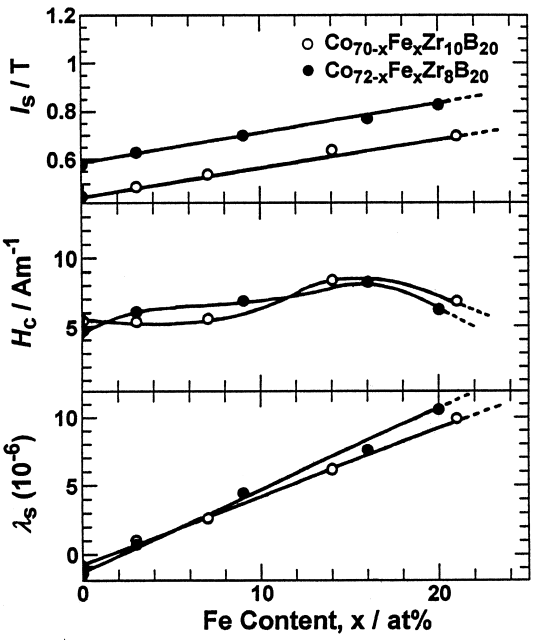

Fig. 22. I_s, H_c and λ_s as a function of Fe content for amorphous $Co_{70-x}Fe_xZr_{10}B_{20}$ and $Co_{72-x}Fe_xZr_8B_{20}$ alloys subjected to annealing for 600 s at 800 K.

those of I_s. The λ_s value is positive and lies in the range of 7–12 $\times$ 10^{-6} for the Nb-containing alloys and 12–15 $\times$ 10^{-6} for the Ta-containing alloys, the value being slightly lower for the former group of alloys. It has been confirmed that T_c also decreases monotonously from 594 to 447 K with increasing Nb content of 0–10 at.% Nb. However, the change in T_c as a function of Ta is slightly different from that for the Nb-containing alloy. That is, T_c decreases significantly to 503 K at 2 at.% Ta and then increases gradually in the Ta content range up to 6 at.% and significantly to 538 K at 8 at.% Ta. The compositional dependence of T_c is analogous to that for I_s and hence an alloy design leading to an increase of T_c is concluded to be an effective method for an increase in I_s. From the compositional dependence of the thermal stability of the supercooled liquid and the magnetic properties, it is concluded that the 2 at.% Nb- or 8 at.% Ta-containing alloy has the combination of high GFA and good soft magnetic properties.

7.1.3. Co–TM–B systems. Figure 22 shows I_s, H_c and λ_s values as a function of Fe content for the $Co_{70-x}Fe_xZr_{10}B_{20}$ and $Co_{72-x}Fe_xZr_8B_{20}$ (x = 0–21 at.%) amorphous alloys [58]. The I_s values increase linearly in the range 0.45–0.83 T with increasing Fe content and with decreasing Zr content, while H_c shows low values of 7 A/m in the range below 10 at.% Fe and increases significantly with a further increase in Fe content. The λ_s value is negative, -1.5×10^{-6} at 0 at.% Fe, changing to positive values on passing through zero at around 2 at.% Fe. The further increase of Fe content causes a linear increase in the positive λ_s, but λ_s is less than 10×10^{-6} even at 20 at.% Fe. It is therefore concluded that the Co-based amorphous alloys containing more than 14 at.% Fe exhibit simultaneously small λ_s values as well as glass transition and a supercooled liquid region before crystallization. Even with the present limited data, it is characterized that $Co_{72-x}Fe_xZr_8B_{20}$ (x = 16–20 at.%) amorphous alloys exhibit good soft magnetic properties of 0.77–0.83 T for I_s, 6.3–8.3 A/m for H_c and 7.6–10 $\times$ 10^{-6} for λ_s, in addition to the appearance of the glass transition phenomenon.

Figure 23 shows μ_e as a function of frequency for the $Co_{63}Fe_9Zr_8B_{20}$ and $Co_{56}Fe_{16}Zr_8B_{20}$ amorphous alloys, together with the data [60,61] of commercial Fe–Si–B and Co–Fe–Ni–Mo–Si–B amorphous alloy sheets. μ_e maintains high values of 17 200–9700 for the former alloy and 18 700–11 200 for the latter alloy in the high-frequency range up to 1 MHz and decreases with a further increase in frequency to 10 MHz. The μ_e values are much higher than those for the Fe–Si–B amorphous alloy over the whole frequency range. Furthermore, the μ_e values of the Co–Fe–Zr–B amorphous alloys are higher than those for the Co–Fe–Ni–Mo–Si–B amorphous alloy with zero λ_s in the high-frequency range above about 100 kHz. The electrical resistiv-

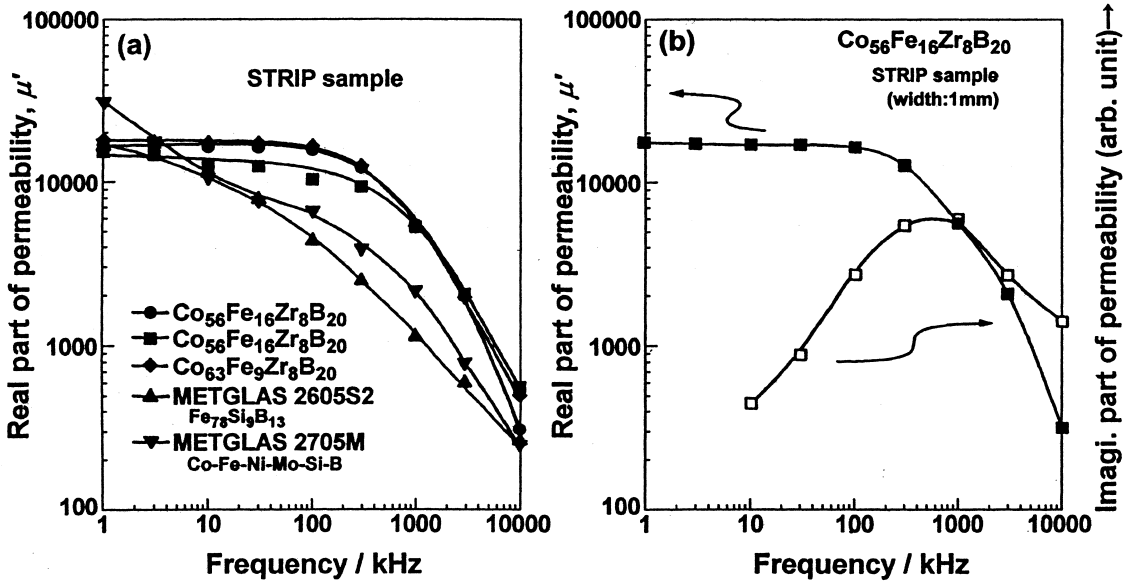

Fig. 23. Frequency dependence of (a) the real (μ′) and (b) the imaginary (μ″) parts of permeability for amorphous $Co_{63}Fe_9Zr_8B_{20}$ and $Co_{56}Fe_{16}Zr_8B_{20}$ alloys of 15 mm width subjected to annealing for 600 s at 750 and 800 K, respectively. The data of conventional Fe–Si–B and Co–Fe–Ni–Mo–Si–B amorphous sheets of 15 mm in width were also shown for comparison.

ities of the $Co_{63}Fe_9Zr_8B_{20}$ and $Co_{56}Fe_{16}Zr_8B_{20}$ amorphous alloys are 1.88 and 1.70 μΩm, respectively, which are higher when compared with 1.34 μΩm for $Co_{71.3}Fe_{4.7}Si_{15}B_{19}$ [60], 1.37 μΩm for $Fe_{78}Si_9B_{13}$ (METGLAS 2605S-2) and 1.42 μΩm for the Co–Fe–Ni–B–Si METGLAS 2714A alloy [61]. Consequently, the excellent high-frequency permeability characteristics of the present amorphous alloys are probably due to the decrease of eddy current loss resulting from the higher electrical resistivities. It is therefore concluded that the present Co-based amorphous alloys have good soft magnetic properties and high stability of supercooled liquid against crystallization.

7.2. Cast bulk amorphous alloys

7.2.1. Fe–(Al,Ga)–(P,C,B,Si) system. The Fe-based amorphous alloys with the large supercooled liquid region of over 60 K before crystallization are expected to have a high GFA which enables us to produce bulk amorphous alloys with diameters above 1 mm by the copper-mold casting process. The cast $Fe_{72}Al_5Ga_2P_{11}C_6B_4$ [66] and $Fe_{72}Al_5Ga_2P_{10}C_6B_4Si_1$ [62,67] amorphous cylinders with diameters of 1–3 mm have been confirmed to have smooth outer surfaces and metallic luster. Besides, the agreement of the outer shape of the cast samples with the inner cavity of the copper mold indicates a good castability of these Fe-based alloys. Even after an appropriate etching treatment, no appreciable contrast corresponding to a crystalline phase is seen over the whole transverse cross-sectional structure of the cast $Fe_{72}Al_5Ga_2P_{10}C_6B_4Si_1$ cylinders with diameters of 1 and 2 mm. In addition, neither cavities nor shrinkage holes are observed, indicating that the amorphous alloy has a good castability owing to the lack of discontinuous change in the specific volume–temperature reaction, which is ordinarily recognized for crystalline alloys obtained from the liquid. The cast $Fe_{72}Al_5Ga_2P_{11}C_6B_4$ amorphous cylinders, with diameters of 0.5–1.5 mm [66], show the sequential changes of the glass transition, supercooled liquid and then single-stage exothermic peak which agree with those of the corresponding melt-spun amorphous ribbon. No distinct changes in the thermal stability and crystallization mode of the supercooled liquid are seen between the cast amorphous cylinders and the melt-spun amorphous ribbon.

The hysteresis *I–H* curve of the cast $Fe_{72}Al_5Ga_2P_{11}C_6B_4$ amorphous cylinder with a diameter of 1 mm was examined in the as-cast and annealed (723 K, 600 s) states [66]. The I_s, H_c and I_r/I_s values of the annealed sample are 1.07 T, 5.1 A/m and 0.37, respectively, indicating that the cast amorphous cylinder has good soft magnetic properties. Besides, the μ_e at 1 kHz for the annealed amorphous cylinder also shows a high value of 7000. The soft magnetic properties were found to be further improved for the 1 at.% Si-containing alloy [62,67]. Figure 24 shows the hysteresis *I–H* curves of the cast $Fe_{72}Al_5Ga_2P_{10}C_6B_4Si_1$ amorphous cylinder with a diameter of 2 mm, together with the data of the cast $Fe_{73}Al_5Ga_2P_{11}C_5B_4$ amorphous cylinder with a diameter of 1 mm. The I_s, H_c and I_r/I_s values for the Si-containing cylinder are

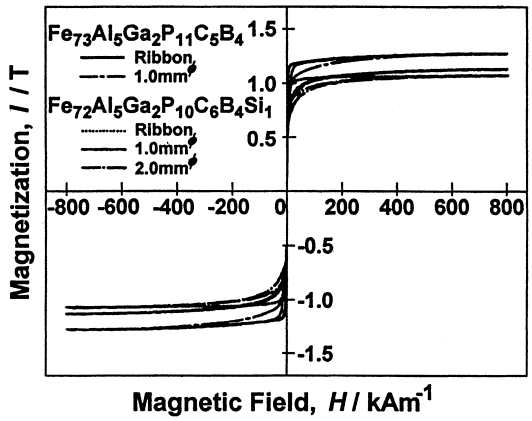

Fig. 24. Hysteresis I–H curves of the cast amorphous $Fe_{73}Al_5Ga_2P_{11}C_5B_4$ and $Fe_{72}Al_5Ga_2P_{10}C_6B_4Si_1$ cylinders with diameters of 1 and 2 mm.

1.14 T, 0.5 A/m and 0.38, respectively. In comparison with those [66] for the Fe–Al–Ga–P–C–B cylinder, H_c decreases and I_r/I_s increases for the Si-containing amorphous cylinder, though I_s decreases slightly owing to the slightly lower Fe concentration. From the thermomagnetic data, it has been confirmed that the cast $Fe_{73}Al_5Ga_2P_{11}C_5B_4$ amorphous cylinder has a T_c at about 600 K which is lower by about 185 K than the crystallization temperature. The T_c value agrees with that determined from the endothermic peak on the DSC curve. It is thus concluded that the cast Fe-based amorphous cylinders with diameters up to 2 mm exhibit good soft magnetic properties of 1.1 T for I_s, 2–6 A/m for H_c and 7000 for μ_e at 1 kHz. When these soft magnetic properties are compared with those for the corresponding melt-spun amorphous ribbons, no distinct changes in I_s and H_c are seen. However, the μ_e value is degraded for the cast cylinder presumably because of the increase in the influence of the demagnetization resulting from the significant change in the sample morphology.

7.2.2. Fe–TM–B systems. Figure 25 shows the outer morphology of the bulk $Fe_{61}Co_7Zr_{10}Mo_5W_2B_{15}$ cylinders with diameters of 3 and 5 mm [68]. These samples have smooth outer surfaces and metallic luster. No contrast of crystalline phase is seen over the whole outer surface. The X-ray diffraction patterns showed a main halo peak with a wave vector K_p (equal to $4\pi \sin\theta/\lambda$) of around 29.6 nm^{-1} and no crystalline peak is observed even for the 5 mm sample. Besides, the optical micrographs of the cross-section of the two samples also revealed a featureless contrast in an etched state using hydrofluoric acid. These results indicate that the bulk cylinders are composed of an amorphous phase in the diameter range up to 5 mm. Considering that the bulk cylinder of 7 mm in diameter consists of an amorphous phase in an outer surface region with a thickness of about 2 mm and of amorphous and crystalline phases in the inner region, the t_{max} for the $Fe_{61}Co_7Zr_{10}Mo_5W_2B_{15}$ alloy is determined to be about 6 mm. It is noticed that the t_{max} is three times larger than the largest value (2 mm for $Fe_{72}Al_5Ga_2P_{10}C_6B_4Si_1$) [62,67] for Fe-based

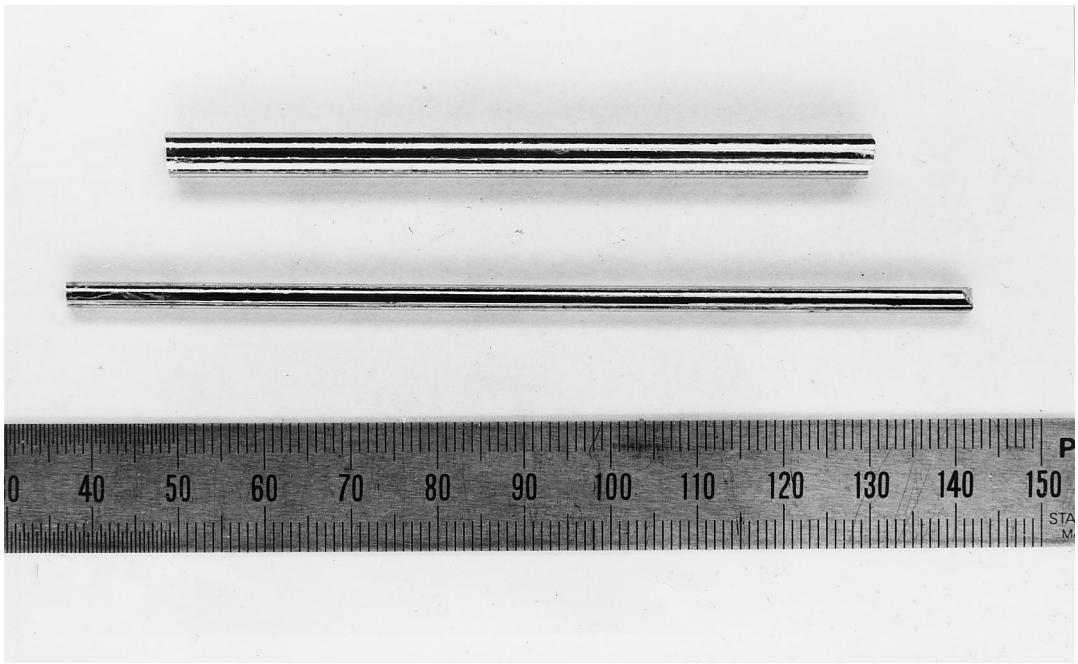

Fig. 25. Outer morphology and surface appearance of cast $Fe_{61}Co_7Zr_{10}Mo_5W_2B_{15}$ alloy cylinders with diameters of 3 and 5 mm.

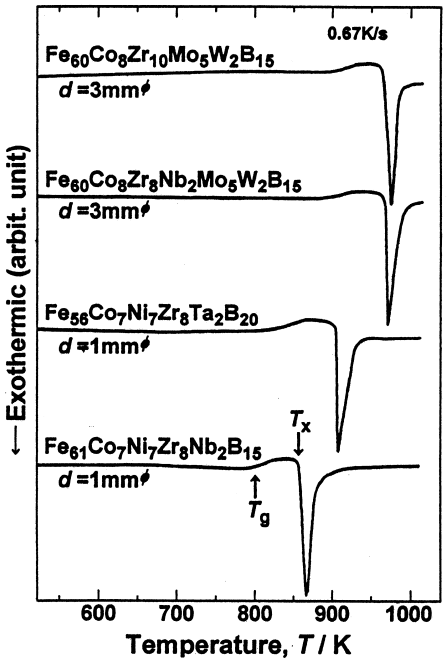

Fig. 26. DSC curves of the cast amorphous $Fe_{61}Co_7Ni_7Zr_8Nb_2B_{15}$, $Fe_{56}Co_7Ni_7Zr_8Ta_2B_{20}$, $Fe_{60}Co_8Zr_8Nb_2Mo_5W_2B_{15}$ and $Fe_{60}Co_8Zr_{10}Mo_5W_2B_{15}$ cylinders with diameters of 1–3 mm.

amorphous alloys reported to date. Figure 26 shows the DSC curves of the bulk amorphous $Fe_{61}Co_7Ni_7Zr_8Nb_2B_{15}$, $Fe_{56}Co_7Ni_7Zr_8Ta_2B_{20}$, $Fe_{60}Co_8Zr_8Nb_2Mo_5W_2B_{15}$ and $Fe_{60}Co_{10}Zr_8Mo_5W_2B_{15}$ cylinders with diameters of 1–3 mm [68]. These amorphous alloys exhibit the sequential transition of glass transition, supercooled liquid and crystallization. The ΔT_x value is as large as 55–88 K and the crystallization occurs by a single exothermic reaction. The crystallites were identified to consist of Fe, Fe_2Zr, Fe_3B, MoB and W_2B phases for the $Fe_{60}Co_8Zr_{10}Mo_5W_2B_{15}$ sample heated to a temperature just above the exothermic peak. The crystallization is due to the simultaneous precipitation of the five crystalline phases. This crystallization mode is in agreement with that [62,66] for other bulk amorphous alloys. The largest ΔT_x is 88 K for $Fe_{56}Co_7Ni_7Zr_8Ta_2B_{20}$, being larger than the largest values (57–67 K) for Fe–(Al,Ga)–(P,C,B,Si) [62,66,67] and nonferrous Pd- and Pt-based amorphous alloys [3].

T_g/T_m was also evaluated. The T_m value was measured at 1420 K for $Fe_{56}Co_7Ni_7Zr_{10}B_{20}$ and 1416 K for $Fe_{61}Co_7Zr_{10}Mo_5W_2B_{15}$ and T_g/T_m was evaluated to be 0.60 for the former alloy and 0.63 for the latter alloy. Considering that T_g/T_m is 0.54 for $Fe_{80}P_{12}B_4Si_4$ [59] and 0.57 for $Fe_{73}Al_5Ga_2P_{11}C_4B_4Si_1$ [62], the present T_g/T_m values are believed to be the highest among all Fe-based amorphous alloys.

Table 7 summarizes t_{max}, T_g, ΔT_x, T_g/T_m, H_v, compressive fracture strength ($\sigma_{c,f}$), I_s, H_c, μ_e at 1 kHz and λ_s for the new amorphous Fe–(Co,Ni)–(Zr,Nb,Ta)–B [11,63–65] and Fe–Co–Zr–(Mo,W)–B alloys [68]. These amorphous alloys exhibit good soft magnetic properties in an annealed (800 K, 300 s) state, i.e. high I_s of 0.74–0.96 T, low H_c of 1.1–3.2 A/m, high μ_e of 12 000–25 000 and low λ_s of $10–14 \times 10^{-6}$. The H_c and μ_e values are superior to those for conventional Fe–Si–B amorphous ribbons [60,61], presumably because of the lower λ_s. Furthermore, the $Fe_{60}Co_8Zr_{10}Mo_5W_2B_{15}$ bulk amorphous alloy has high $\sigma_{c,f}$ of 3800 MPa and H_v of 1360 which exceed largely those ($\sigma_{c,f}$ = 1000–2000 MPa, H_v = 300–800) [33] for high-carbon high-alloy tool steels and 25 mass% Ni maraging steel. No bulk alloys with high strength above 3000 MPa for $\sigma_{c,f}$ and 1000 for H_v have been obtained for any kinds of Fe-based alloys including amorphous and crystalline phases. Besides, no weight loss is detected after immersion for 3.6 ks at 298 K in aqua regia. It is therefore concluded that the Fe-based bulk amorphous alloys possess simultaneously high GFA, high strength, high corrosion resistance and good soft magnetic properties, which cannot be obtained for other amorphous and crystalline alloys.

8. NANOSTRUCTURED BULK AMORPHOUS ALLOYS

8.1. Formation and structures

The single-stage crystallization mode typical for bulk amorphous alloys also implies that the amorphous phase containing homogeneously nanocrystalline particles is not formed. It has previously been pointed out that the mixed structure consisting

Table 7. Maximum sample thickness, thermal stability, Vickers hardness, compressive strength and magnetic properties of the Fe–(Co,Ni)–(Zr,Nb,Ta)–B and Fe–(Co,Ni)–Zr–(Mo,W)–B amorphous alloys

Alloy[a]	t_{max} (mm)	T_g (K)	ΔT_x (K)	T_g/T_m	H_v	$\sigma_{c,f}$ (MPa)	I_s (T)	H_c (A/m)	μ_e (kHz)	λ_s (10^{-6})
(a)	2	814	73	0.60	1370	–	0.96	2.0	19 100	10
(b)	2	828	86	–	1370	–	0.75	1.1	25 000	13
(c)	2	808	50	–	1340	–	0.85	3.2	12 000	14
(d)	2	827	88	–	1360	–	0.74	2.6	12 000	14
(e)	6	898	64	0.63	1360	3800	–	–	–	14

[a] (a) $Fe_{56}Co_7Ni_7Zr_{10}B_{20}$; (b) $Fe_{56}Co_7Ni_7Zr_8Nb_2B_{20}$; (c) $Fe_{61}Co_7Ni_7Zr_8Nb_2B_{15}$; (d) $Fe_{56}Co_7Ni_7Zr_8Ta_2B_{20}$; (e) $Fe_{60}Co_8Zr_{10}Mo_5W_2B_{15}$.

of nanoscale crystalline particles embedded in an amorphous phase is formed in the satisfaction of the four following criteria [69]:

1. multistage crystallization process;
2. existence of homogeneous nucleation sites in an amorphous phase;
3. suppression of growth reaction caused by segregation of a solute element with low atomic diffusivity at the nanocrystal/amorphous interface; and
4. high thermal stability of the remaining amorphous phase by the enrichment of solute elements from the primary crystalline phase.

With the aim of changing the single-stage crystallization mode to the nanocrystallization mode in the maintenance of the supercooled liquid region, we examined the effect of additional M (M = Ag, Ti, Nb, Pd, Au or Pt) elements on the formation of the nanocrystalline structure for the Zr–Al–Ni–Cu amorphous alloys [70–73]. The additional elements were chosen because of positive heats of mixing (ΔH_{mix}) against the other constituent elements for Ag and Nb, a nearly zero ΔH_{mix} against Zr for Ti, and extremely large negative ΔH_{mix} against Zr for Pd, Au and Pt [32]. The addition of the elements with positive, nearly zero and largely negative values of ΔH_{mix} causes the deviation of the three empirical rules in the alloy components. As a result, microscopic heterogeneity in the structure and alloy component generates, leading to the precipitation of a primary crystalline phase from the amorphous matrix.

Figure 27 shows the DSC curves of the Zr–Al–Ni–Cu amorphous alloys containing Ag, Ti or Pd, together with the data of the Zr–Al–Ni–Cu alloy. The addition of all the elements causes the change from the single-stage crystallization mode to the two-stage crystallization mode in the maintenance of the supercooled liquid region before crystallization. The structure of the alloys annealed for different periods at the temperatures just below the onset temperature of the first exothermic reaction (T_{x1}) was examined by TEM. As shown in Fig. 28, the Pd- and Ti-containing alloys consist of nanoscale crystalline precipitates embedded in the amorphous matrix, indicating the effectiveness of the additional elements on the formation of the nanostructured amorphous phase. The precipitates appear to have a spherical morphology and their particle size is measured to be 5–10 nm for the Pd-containing alloy and 10–15 nm for the Ti-containing alloy. Furthermore, the redistribution behavior of alloy components by the precipitation of the primary crystalline phase was examined for the Ag-, Nb- and Pd-containing alloys by the nanobeam EDS technique. The EDS profiles indicate a common feature that the Al element, which plays a dominant role in the high stability of the supercooled liquid, is enriched into the remaining amorphous phase

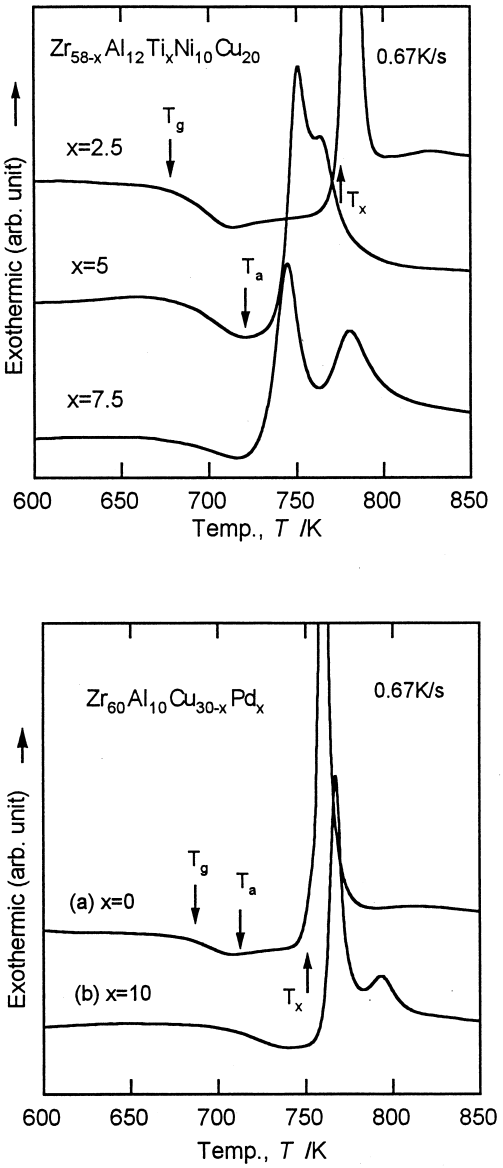

Fig. 27. DSC curves of Zr–Al–Ti–Ni–Cu and Zr–Al–Cu–Pd amorphous alloys.

accompanying the significant segregation of Al in the amorphous phase just near the nanocrystal/amorphous interface. This is consistent with the previous interpretation that the redistribution of Al around Zr is essential for the progress of crystallization for the Zr–Al–Ni–Cu amorphous alloys.

The precipitation behavior of the nanoscale Zr_2Cu phase was also examined by some kinetic analyses [73]. Figure 29 shows the change in the first exothermic peak due to the precipitation of the Zr_2(Cu,Pd) phase during isothermal annealing at different temperatures for the $Zr_{60}Al_{10}Cu_{20}Pd_{10}$ amorphous alloy. With increasing annealing temperature, the peak position shifts to a shorter time side and the peak intensity increases monotonously.

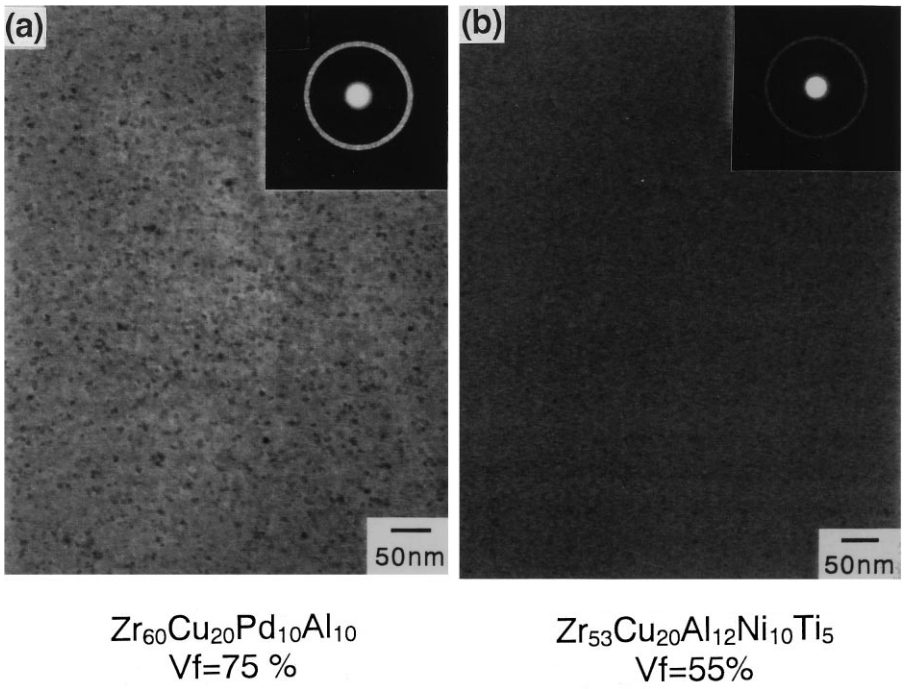

Fig. 28. Bright-field electron micrograph and selected-area electron diffraction patterns of Zr-based amorphous alloys annealed at temperatures just below the first exothermic reaction.

The transformation ratio (y) corresponding to the crystalline fraction (V_f), from the amorphous to Zr_2Cu phase as a function of isothermal annealing time (t_a) excluding the incubation time, increases along the sigmoidal curve. The y values between 0.1 and 0.9 were used for the subsequent analysis in the framework of the Johnson–Mehl–Avrami equation [74]. In the relationship between $\ln[-\ln(1-y)]$ and $\log(t)$ at various annealing temperatures, a good linear correlation is recognized at all annealing temperatures and the slope corresponds to the Avrami exponent (the n value). The n value is evaluated to be 3.4–3.6. The n value allows us to presume that the crystallization proceeds by the diffusion-controlled growth reaction in which all precipitates growing from small dimensions have an increasing nucleation rate [75,76]. We also measured the activation energy for the first-stage crystallization reaction corresponding to the precipitation of the nanocrystalline phase by the Arrhenius plot of the isothermal annealing data and the Kissinger plot of the continuous heating data. The activation energy is 3.2–3.6 eV, which is much larger than those (1.9–2.2 eV) for the Zr–Al–Ni–Cu and Zr–Al–Cu alloys without nanocrystalline phase, indicating that the formation of the nanostructure is partly due to the difficulty of the crystallization reaction caused by the necessity of the much higher activation energies.

8.2. Mechanism for formation of the nanostructured amorphous phase

It has been reported that the crystallized structure of the $Zr_{65}Al_{7.5}Cu_{27.5}$ alloy caused by the polymorphic reaction consists of Zr_2Cu phase with large grain sizes of 400–500 nm, while the addition of Pd or Au decreases drastically the grain size of the $Zr_2(Cu,Pd)$ phase to less than 10 nm [71,73]. The high-resolution TEM and nanobeam EDX analyses reveal that the Pd and Au are dissolved into the Zr_2Cu phase and the Al is rejected from the compound phase and segregated into the remaining amorphous phase. The Avrami exponent values indicate that the nanocrystallization of the Pd- and Au-containing alloys proceeds by the diffusion-controlled growth reaction in which all precipitates

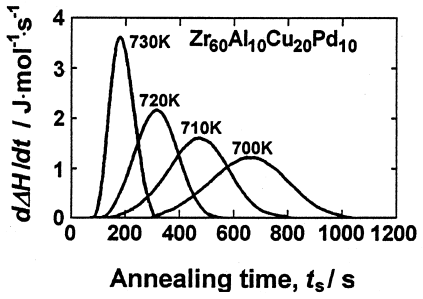

Fig. 29. Change in the DSC curves due to crystallization with respect to isothermal annealing time at different temperatures for $Zr_{60}Al_{10}Cu_{20}Pd_{10}$ amorphous alloy.

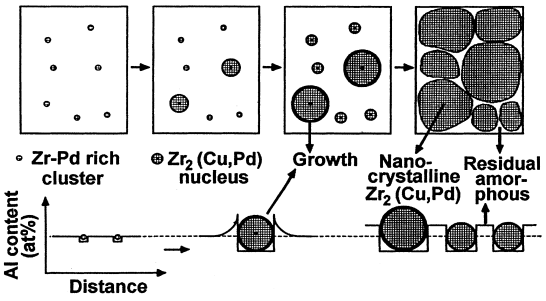

Fig. 30. Schematic illustration showing the formation process of the nanocrystalline $Zr_2(Cu,Pd)$ phase surrounded by residual amorphous phase and showing the change in the Al concentration in the $Zr_2(Cu,Pd)$ and remaining amorphous phases during isothermal annealing.

growing from small dimensions have an increasing nucleation rate. We have also shown that the activation energy for the first-stage crystallization reaction corresponding to the precipitation of the nanocrystalline phase is 3.2–3.6 eV for the $Zr_{60}Al_{10}Cu_{20}Pd_{10}$ alloy and 3.2–3.8 eV for the $Zr_{60}Al_{10}Cu_{22}Au_8$ alloy, which are much larger than that value (1.9–2.2 eV) for the Zr–Al–Cu ternary alloy. Based on the above-described experimental results on the structural and kinetic analyses of crystallization, the formation process of the nanoscale $Zr_2(Cu,Pd)$ phase surrounded by a residual amorphous phase upon partial crystallization of the Zr–Al–Cu–Pd amorphous alloys is schematically shown in Fig. 30 [73]. It is generally known that the formation of a nanostructure from an amorphous phase requires the four criteria described in Section 8.1. The addition of Pd or Au with much larger negative ΔH_{mix} against Zr causes the change of the crystallization mode from the single stage to the two stages as well as the homogeneous generation of Zr–Pd-rich clusters, which can act as a nucleation site of the $Zr_2(Cu,Pd)$ phase. The subsequent growth of the Zr–Pd-rich cluster is also difficult because of the enrichment of Al in the remaining amorphous phase near the interface between amorphous and $Zr_2(Cu,Pd)$ phases resulting from the elimination of Al from the $Zr_2(Cu,Pd)$ phase. The difficulty of the growth reaction seems to result in the high activation energy for the precipitation of the $Zr_2(Cu,Pd)$ phase. Furthermore, the enrichment of Al also induces an increase of the thermal stability of the remaining amorphous phase against crystallization. The increase of the thermal stability also plays an important role in the maintenance of the nanoscale size of the primary crystalline phase.

8.3. Mechanical properties and deformation behavior of bulk nanostructured amorphous alloys

Figure 31 shows the σ_f, E and H_v as a function of volume fraction (V_f) of the primary crystalline phase for the melt-spun Pd-containing alloy [73] subjected to heating for different periods at a temperatures just below T_{x1} in the supercooled liquid region, followed by water-quenching. With increasing V_f, E and H_v increase almost linearly in the wide V_f range up to about 75% where good bending ductility is maintained. However, the transition from ductile to brittle nature at $V_f = 75\%$ causes a significant decrease in V_f, though E and H_v increase further. It is noticed that good ductility is maintained even in the high V_f range up to 75%. The similar changes in σ_f, E and H_v with V_f are also recognized for the cast bulk nanostructured amorphous alloys containing Pd, as shown in Fig. 32. However, the ductile/brittle transition occurs at small V_f of 30–40% and the linear increase in V_f stops in the vicinity of the transitional V_f value. The maximum increasing amount in V_f is approxi-

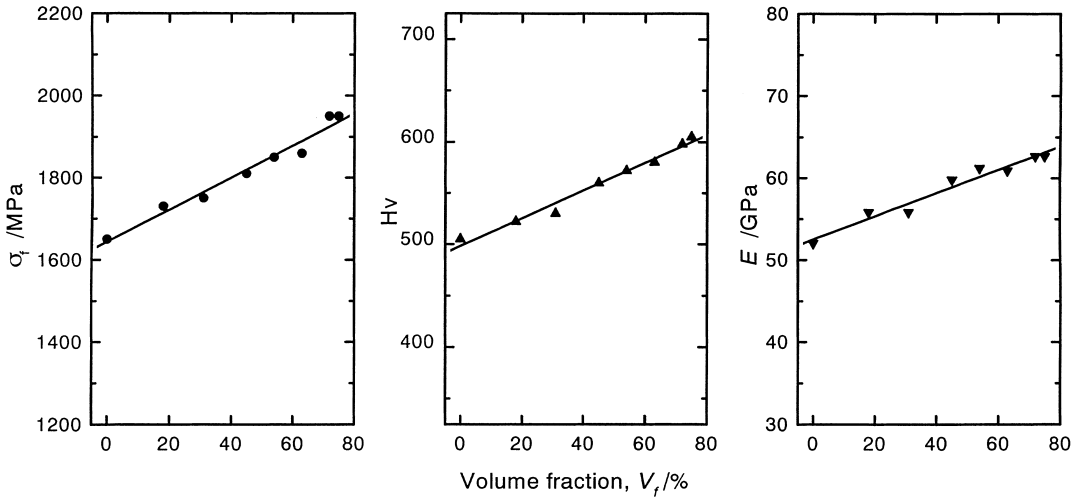

Fig. 31. Changes in σ_f, H_v and E with V_f of compounds for a melt-spun $Zr_{60}Al_{10}Cu_{20}Pd_{10}$ amorphous alloy.

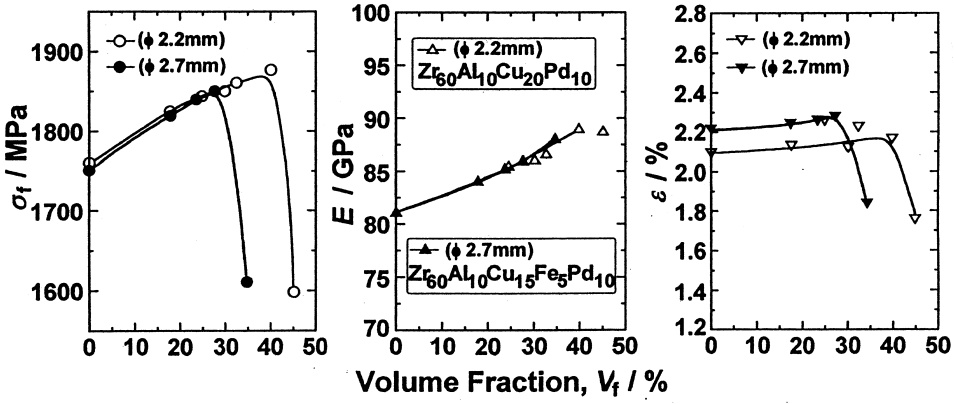

Fig. 32. Changes in σ_f, E and H_v with V_f of compounds for cast bulk amorphous Zr–Al–Ni–Cu–Pd amorphous alloys.

mately 30% and the highest V_f is 1980 MPa for the Pd-containing alloy. The V_f of the mixed-phase alloy has been interpreted by the simple mixture rule between the amorphous matrix and the nanoscale compound. Tensile fracture occurs along the maximum shear plane, which is declined by about 45° to the direction of tensile load and the fracture surface consists mainly of a vein pattern, as exemplified by the Pd-containing alloy in Fig. 33. There is no distinct difference in the feature of tensile fracture behavior between the bulk nanostructured amorphous alloys and amorphous single-phase alloys. The similar fracture mode indicates that the intergranular amorphous phase keeps good ductile nature and the fracture occurs preferentially along the intergranular amorphous region, as illustrated in Fig. 34. The shear deformation, which is limited to the narrow width of 20–30 nm, can be effectively suppressed by the nanocrystalline (compound) particles with higher H_v and/or higher yield strength, leading to the increase in V_f. In this deformation and fracture mechanism, the remaining amorphous alloy must keep good ductility, which is comparable to the as-cast amorphous phase. The maintenance of the good ductility seems to result from the residual existence of the supercooled liquid region before crystallization for the remaining amorphous phase. The present annealing was made by heating in the supercooled liquid region, followed by water-quenching, which is capable of introducing a large amount of free volume. The decrease in the critical V_f of the ductile/brittle transition for the bulk alloy is presumably due to the difficulty in the re-entrance of free volumes owing to much lower cooling rates for the bulk alloys than for the ribbon alloys.

More recently, the good ductility of the bulk nanostructured amorphous alloys has been confirmed by the appearance of slipping-off-type fracture mode for the bulk sample subjected to a compressive test at room temperature [77]. As an example, Fig. 35 shows the compressive stress–elongation curves of the $Zr_{60}Al_{10}Cu_{20}Pd_{10}$ cylindrical samples in as-cast amorphous single-phase and nanostructured amorphous-phase states. Although the amorphous single-phase alloy exhibits a high yield strength of 1770 MPa and a small plastic elongation of about 0.4%, the elongation increases remarkably to about 2.5% for the nanostructured amorphous alloy. The absence of data on the stress–elongation curve in the larger elongation

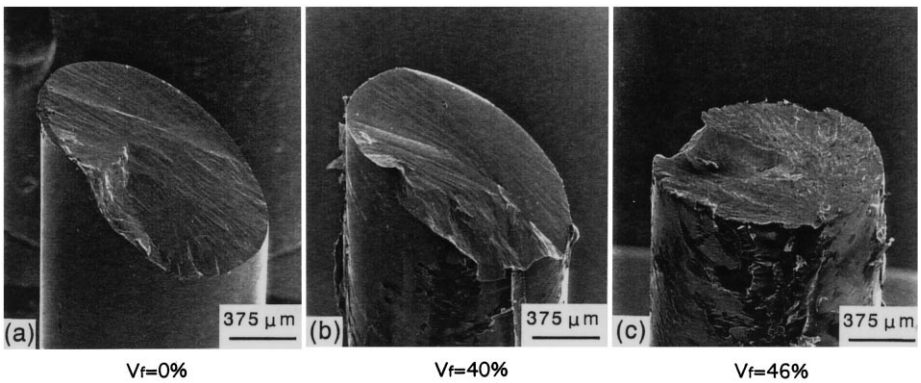

Fig. 33. Tensile fracture surface appearance of the cast bulk amorphous $Zr_{60}Al_{10}Cu_{20}Pd_{10}$ alloy: (a) $V_f = 0\%$; (b) $V_f = 40\%$; and (c) $V_f = 46\%$.

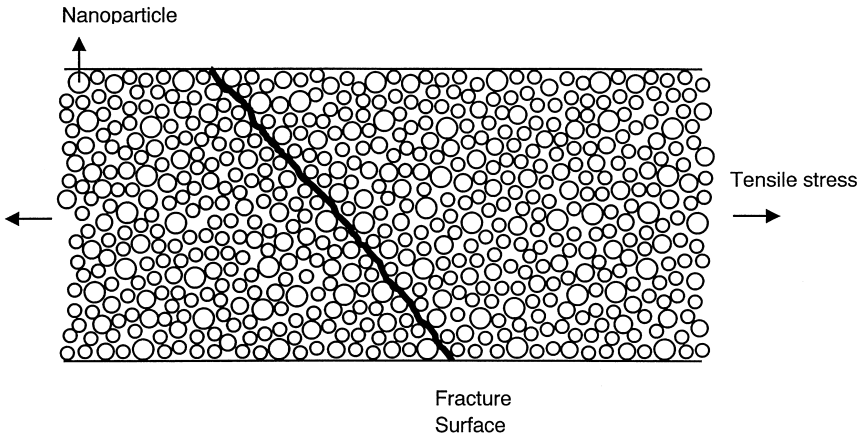

Fig. 34. Schematic illustration of tensile fracture mode for the nanocrystalline amorphous alloys exhibiting improved mechanical properties.

range above 2.5% does not imply fracture of the specimen and results from damage to the strain gauge used in the measurement. Figure 36 shows the outer appearance of the nanostructured amorphous alloy subjected to the plastic elongation of 2.5%. A distinct slip step is seen along the maximum shear plane, which is declined by about 50° to the direction of the uniaxial compressive load. We have also confirmed that the vein pattern in the fracture surface of the nanostructured amorphous alloy is in a more developed and distinct state as compared with the corresponding amorphous single-phase alloy. The more distinct vein pattern is presumably because the shear sliding stress is localized to the intergranular amorphous-phase field and the localization causes a more distinct sliding deformation through the softening phenomenon caused by the increase in temperature.

9. FORMATION AND MECHANICAL PROPERTIES OF BULK-CLUSTERED AMORPHOUS ALLOYS

It was shown in the previous section that the most important point in obtaining high V_f for the mixed-phase alloys is attributed to the good ductility of the remaining amorphous phase. The above-described nanostructured amorphous alloys were obtained by annealing-induced partial crystallization in the supercooled liquid region, followed by water-quenching. In addition to the annealing treatment, as another route to producing the similar nanostructured amorphous structure, one can observe a control method of cooling rate from the liquid during casting into a bulk amorphous alloy.

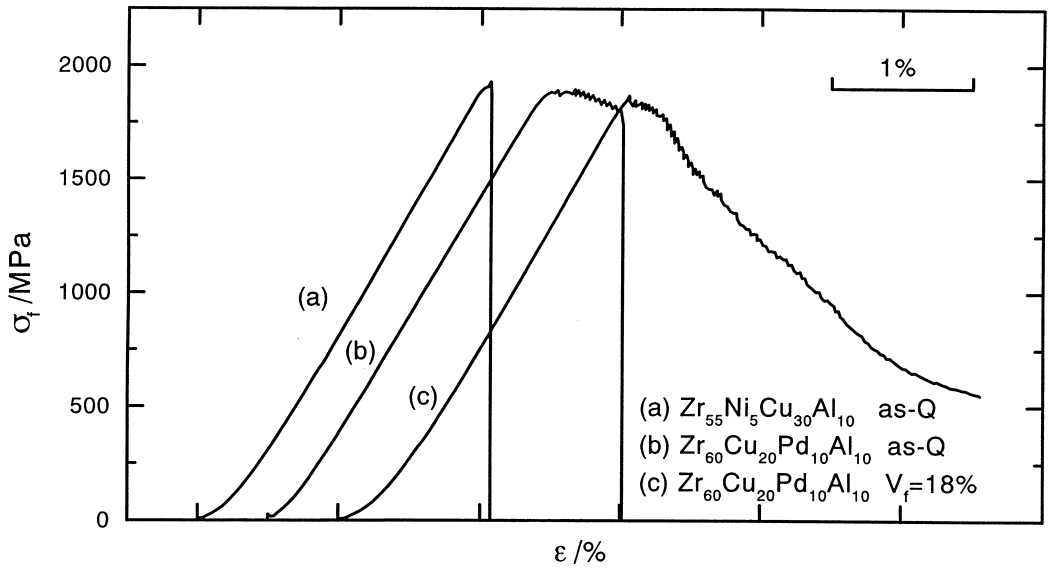

Fig. 35. Compressive stress–strain curves of $Zr_{60}Cu_{20}Pd_{10}Al_{10}$ and $Zr_{55}Ni_5Cu_{30}Al_{10}$ cylindrical rods in as-cast amorphous and nanocrystalline mixed-phase states.

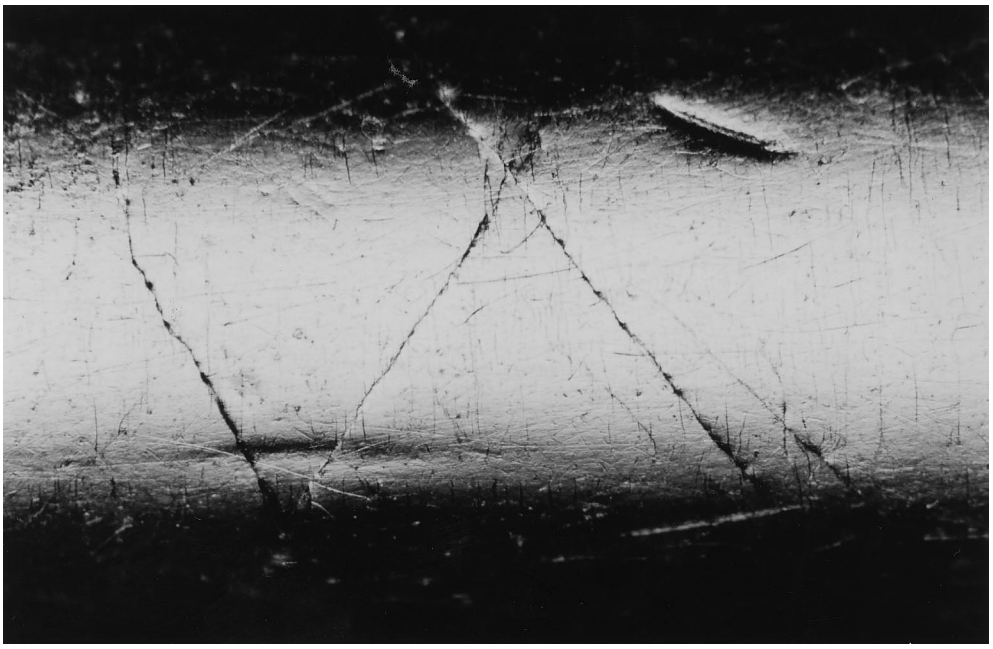

Fig. 36. Outer surface appearance of the nanocrystalline amorphous alloy rod subjected to plastic elongation of 2.5%.

The control method was expected to result in the homogeneous dispersion of much smaller precipitates in an amorphous matrix containing a much larger amount of free volume [47,78]. Figure 37 shows small-angle scattering X-ray diffraction patterns of amorphous single phase and mixed phases in the as-cast state for the $Zr_{60}Al_{10}Ni_{10}Cu_{19}Nb_1$ alloy. The mixed structure was produced by controlling the casting temperature. Some broad and low-intensity diffraction peaks are seen at the positions corresponding to Zr_2Cu. From the high-resolution TEM image taken from the mixed-structure alloy, the compound phase has been identified to have a grain size of about 4 nm and an interparticle spacing of about 6 nm. The crystalline particles are much smaller than those for the nanostructured amorphous alloys obtained by annealing and hence the structure obtained by the controlling process is named as a clustered amorphous alloy.

Figure 38 shows the flexural stress–deflection curves of the clustered amorphous Zr–Cu–Al–Ni–Nb alloy, together with the data of the corresponding amorphous single and nanostructured alloys. It is noticed that the bending flexural strength is 4300 MPa for the clustered amorphous alloy, being much higher as compared with 2000 MPa for the amorphous single-phase alloy and 3300 MPa for the nanostructured amorphous alloy. The V_f of the precipitates in the clustered amorphous alloy is estimated to be 30%, which is considerably smaller than that for the nanostructured alloy, though the particle size is much smaller. The remarkable increase in the flexural strength cannot be explained by the mixture rule. The reason for the increase in flexural strength is presumably due to the generation of residual compressive stress in the amorphous region just near the clustered particles resulting from the high cooling rate from the melt owing to the difference in the coefficients of thermal expansion between the two phases [78]. The finding that the clustered amorphous alloy with the extremely high strength is formed by control of the cooling rate is expected to

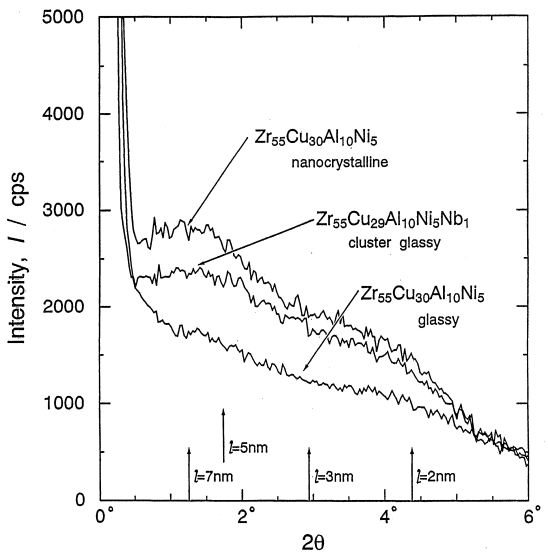

Fig. 37. Small-angle X-ray scattering profile of the clustered amorphous $Zr_{55}Cu_{29}Al_{10}Ni_5Nb_1$ alloy. The data of Zr-based amorphous and nanocrystalline alloys are also shown for comparison.

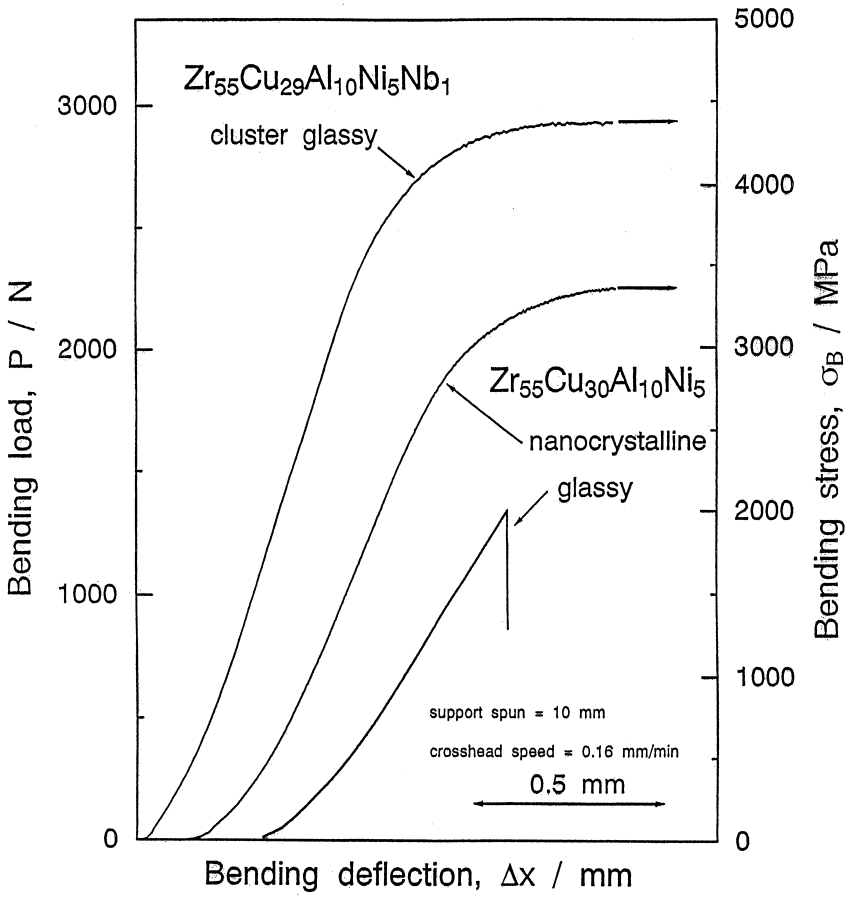

Fig. 38. Bending flexural stress and deflection curves of the clustered amorphous $Zr_{55}Al_{10}Ni_5Cu_{29}Nb_1$ alloy. The data of amorphous and nanocrystalline Zr-based alloys are also shown for comparison.

be widely used as a new strengthening mechanism for bulk amorphous alloys.

10. APPLICATIONS AND CONCLUSIONS

Table 8 summarizes fields of application in which the bulk amorphous alloys have expected uses. As particularly important application fields, one can list machinery/structural materials, magnetic materials, acoustic materials, somatologic materials, optical machinery materials, sporting goods materials and electrode materials. Finally, it is pleasing to introduce a successful example of a real application of bulk amorphous alloys as sporting goods materials. As exemplified in Fig. 39, the Zr–Al–Ni–Cu and Zr–Ti–Al–Ni–Cu bulk amorphous alloys have already been used as face materials in golf clubs [79, 80]. The practical use results from the experimental results that the Zr-based bulk amorphous alloys have simultaneously high tensile strength, high bending strength, high hardness, high fracture toughness, high impact fracture energy, high fatigue strength, good castability, good cutting machinability and good corrosion resistance. Bulk amorphous alloys have also been tested as optical machinery materials (Zr–Al–Ni–Cu alloy) and as an electrode material (Pd–Cu–Ni–P alloy) and are expected to join the group of real application materials. Considering the recent significant extension of application fields, it is expected that the importance of bulk amorphous alloys as basic science and

Table 8. Application fields for bulk amorphous alloys which are expected to be used as engineering materials

Fundamental characteristic	Application field
High strength	Machinery structural materials
High hardness	Optical precision materials
High fracture toughness	Die materials
High impact fracture energy	Tool materials
High fatigue strength	Cutting materials
High elastic energy	Electrode materials
High corrosion resistance	Corrosion resistant materials
High wear resistance	Hydrogen storage materials
High viscous flowability	Ornamental materials
High reflection ratio	Composite materials
Good soft magnetism	Writing appliance materials
High frequency permeability	Sporting goods materials
High magnetostriction	Bonding materials
Efficient electrode (Chlorine gas)	Soft magnetic materials
High hydrogen storage	High magnetostrictive materials

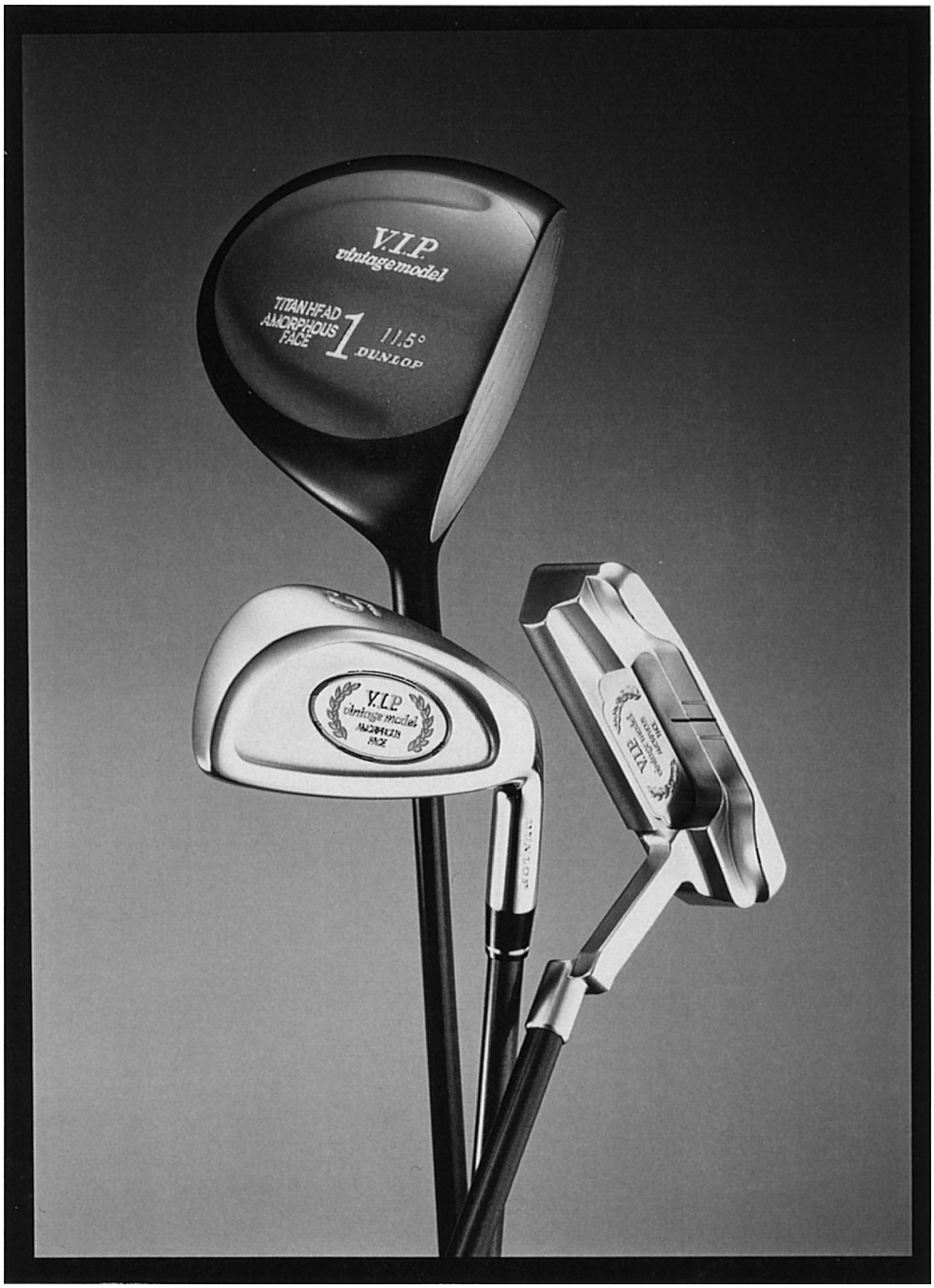

Fig. 39. Outer shapes of commercial golf clubs in wood-, iron- and putter-type forms where the face materials are composed of Zr–Al–Ni–Cu bulk amorphous alloys.

engineering materials will increase steadily in the 21st century.

Acknowledgements—This work is partly supported by the Inoue Superliquid Glass Project of Exploratory Research for Advanced Technology, Japan Science and Technology Corporation (JST).

REFERENCES

1. Klement, W., Willens, R. H. and Duwez, P., *Nature*, 1960, **187**, 869.
2. Cahn, R. W., in *Rapidly Solidified Alloys*, ed. H. H. Libermann. Marcel Dekker, New York, 1993, p. 1.
3. Chen, H. S., *Rep. Prog. Phys.*, 1980, **43**, 353.
4. Kui, H. W., Greer, A. L. and Turnbull, D., *Appl. Phys. Lett.*, 1984, **45**, 615.

5. Kui, H. W. and Turnbull, D., *Appl. Phys. Lett*., 1985, **47**, 796.
6. Inoue, A., Ohtera, K., Kita, K. and Masumoto, T., *Japan. J. appl. Phys*., 1988, **27**, L2248.
7. Inoue, A., Zhang, T. and Masumoto, T., *Mater. Trans. Japan. Inst. Metals*, 1989, **30**, 965.
8. Inoue, A., Zhang, T. and Masumoto, T., *Mater. Trans. Japan. Inst. Metals*, 1990, **31**, 177.
9. Peker, A. and Johnson, W. L., *Appl. Phys. Lett*., 1993, **63**, 2342.
10. Inoue, A. and Gook, J. S., *Mater. Trans. Japan. Inst. Metals*, 1995, **36**, 1180.
11. Inoue, A., Zhang, T., Itoi, T. and Takeuchi, A., *Mater. Trans. Japan. Inst. Metals*, 1997, **38**, 359.
12. Inoue, A., Nishiyama, N. and Matsuda, T., *Mater. Trans. Japan. Inst. Metals*, 1996, **37**, 181.
13. Schwarz, R. B. and He, Y., *Mater. Sci. Forum*, 1997, **235–238**, 231.
14. Zhang, T. and Inoue, A., *Mater. Trans. Japan. Inst. Metals*, 1998, **39**, 1001.
15. Zhang, T. and Inoue, A., *Mater. Trans. Japan. Inst. Metals*, 1999, **40**, 301.
16. Akatsuka, R., Zhang, T., Koshiba, M. and Inoue, A., *Mater. Trans. Japan. Inst. Metals*, 1999, **40**, 258.
17. Inoue, A., *Mater. Trans. Japan. Inst. Metals*, 1995, **36**, 866.
18. Inoue, A., *Mater. Sci. Engng*, 1997, **A226–228**, 357.
19. Inoue, A., Zhang, T. and Takeuchi, A., *Mater. Sci. Forum*, 1998, **269–272**, 855.
20. Inoue, A., Takeuchi, A. and Zhang, T., *Metall. Mater. Trans*., 1998, **29A**, 1779.
21. Inoue, A., *Bulk Amorphous Alloys*. Trans Tech Publications, Zurich, 1998.
22. Inoue, A. and Nishiyama, N., *Mater. Sci. Engng*, 1997, **A226–228**, 401.
23. Inoue, A., in *Handbook on the Physics and Chemistry of Rare Earths*, Vol. 24, ed. K. A. Gschneidner Jr and L. Eyring. North-Holland, Amsterdam, 1997, p. 83.
24. Patent 1989, No. 7-122120.
25. Inoue, A., Shibata, T. and Zhang, T., *Mater. Trans. Japan. Inst. Metals*, 1995, **36**, 1420.
26. Zhang, T., Inoue, A. and Masumoto, T., *Mater. Sci. Engng*, 1994, **A181–182**, 1423.
27. Inoue, A. and Zhang, W., *J. appl. Phys*., 1999, **85**, 000.
28. Inoue, A., Wang, X.M. and Yoshii, I., *Mater. Trans. Japan. Inst. Metals*, 1999, **40**, 1130.
29. Inoue, A., Negishi, T., Kimura, H. M., Zhang, T. and Yavari, A. R., *Mater. Trans. Japan. Inst. Metals*, 1998, **39**, 318.
30. Masumoto, T. (ed.), *Material Science of Amorphous Alloys*. Ohmu, Tokyo, 1983, p. 39.
31. Matsubara, E., Tamura, T., Waseda, Y., Inoue, A., Zhang, T. and Masumoto, T., *J. Non-Cryst. Solids*, 1992, **150**, 380.
32. de Boer, F. R., Boom, R., Mattens, W. C. M., Miedema, A. R. and Niessen, A. K., *Cohesion in Metals*. North-Holland, Amsterdam, 1989.
33. Japan Institute of Metals, in *Metals Databook*. Maruzen, Tokyo, 1983, p. 8.
34. Li, H. Doctoral thesis, Tohoku University, Japan, 1998.
35. Inoue, A., Nakamura, T., Nishiyama, N. and Masumoto, T., *Mater. Trans. Japan. Inst. Metals*, 1992, **33**, 937.
36. Inoue, A., Nakamura, T., Sugita, T., Zhang, T. and Masumoto, T., *Mater. Trans. Japan. Inst. Metals*, 1993, **34**, 351.
37. Inoue, A. and Zhang, T., *Mater. Trans. Japan Inst. Metals*, 1996, **37**, 185.
38. Inoue, A., Zhang, T. and Takeuchi, A., *Appl. Phys. Lett*., 1997, **71**, 464.
39. Inoue, A., Nishiyama, N. and Kimura, H. M., *Mater. Trans. Japan. Inst. Metals*, 1997, **38**, 179.
40. Zhang, T. and Inoue, A., *Mater. Trans. Japan. Inst. Metals*, 1998, **39**, 857.
41. Yokoyama, Y., Nishiyama, N., Fukaura, K., Sunada, H. and Inoue, A., *Mater. Trans. Japan. Inst. Metals*, 1999, **40**, 696.
42. Ogura, T., Masumoto, T. and Fukushima, K., *Scripta metall*., 1975, **9**, 979.
43. Izumi, H., Sunada, H. and Hayashi, Y., *J. Japan. Inst. Metals*, 1984, **48**, 371.
44. Askeland, D. R., in *Science and Engineering of Materials*. PWS Publishing, Boston, 1994, p. 152.
45. Gilbert, C. J., Ritchie, R. O. and Johnson, W. L., *Appl. Phys. Lett*., 1997, **71**, 464.
46. Gilbert, C. J., Schroeder, V. and Ritchie, R. O., *Metall. Mater. Trans*., 1999, **30A**, 1739.
47. Yokoyama, Y., Yamano, K., Fukaura, H., Sunada, H. and Inoue, A., *Mater. Trans. Japan. Inst. Metals*, 1999, **40**, 1382.
48. Asami, K. and Inoue, A., *Mater. Sci. Engng*, to be submitted.
49. Nishiyama, N. and Inoue, A., *Mater. Trans. Japan. Inst. Metals*, 1999, **40**(1), 64.
50. Kawamura, Y., Kato, H., Inoue, A. and Masumoto, T., *Int. J. Powder Metall*., 1997, **33**(2), 50.
51. Inoue, A., Kawamura, Y. and Saotome, Y., *Mater. Sci. Forum*, 1997, **233–234**, 147.
52. Bhatti, A. R. and Cantor, B., *Mater. Sci. Engng*, 1988, **97**, 479.
53. Inoue, A. and Saotome, Y., *Metals*, 1993, **3**, 51.
54. Kato, H., Chen, H.S. and Inoue, A., to be submitted.
55. Zhang, T., Tsai, A. P., Inoue, A. and Masumoto, T., *Boundary*, 1991, **7**(9), 39.
56. Zhang, T. and Inoue, A., unpublished research, 1997.
57. Inoue, A. and Katsuya, A., *Mater. Trans. Japan. Inst. Metals*, 1996, **37**, 1332.
58. Inoue, A., Koshiba, M., Itoi, T. and Makino, A., *Appl. Phys. Lett*., 1998, **73**, 744.
59. Inoue, A. and Park, R. E., *Mater. Trans. Japan. Inst. Metals*, 1996, **37**, 1715.
60. Masumoto, T. (ed.), *Materials Science of Amorphous Alloys*. Ohmu, Tokyo, 1983, p. 97.
61. Smith, C. H., in *Rapidly Solidified Alloys*, ed. H. H. Liebermann. Marcel Dekker, New York, 1993, p. 617.
62. Inoue, A., Murakami, A., Zhang, T. and Takeuchi, A., *Mater. Trans. Japan. Inst. Metals*, 1997, **38**, 189.
63. Inoue, A., Koshiba, M., Zhang, T. and Makino, A., *Mater. Trans. Japan. Inst. Metals*, 1997, **38**, 577.
64. Inoue, A., Koshiba, M., Zhang, T. and Makino, A., *J. appl. Phys*., 1998, **83**, 1967.
65. Inoue, A. and Makino, A., *Soft Magnet. Mater*., 1998, **8**, 3.
66. Inoue, A., Shinohara, Y. and Gook, J. S., *Mater. Trans. Japan. Inst. Metals*, 1995, **36**, 1427.
67. Inoue, A., *Mater. Sci. Engng*, 1997, **A226–228**, 357.
68. Inoue, A., Zhang, T. and Takeuchi, A., *Appl. Phys. Lett*., 1997, **71**, 464.
69. Inoue, A., *Nanostruct. Mater*., 1995, **6**, 53.
70. Inoue, A., Zhang, T. and Kim, Y. H., *Mater. Trans. Japan Inst. Metals*, 1997, **38**, 749.
71. Fan, C. and Inoue, A., *Mater. Trans. Japan Inst. Metals*, 1997, **38**, 1040.
72. Inoue, A., Fan, C. and Takeuchi, A., *Adv. Mater*., 1998, **4**, 373.
73. Fan, C. and Inoue, A., *Mater. Trans. Japan Inst. Metals*, 1999, **40**, 42.
74. Johnson, W. A. and Mehl, R. F., *Trans. Am. Inst. Min. Engrs*, 1939, **135**, 416.
75. Ham, F. S., *J. appl. Phys*., 1959, **30**, 915.

76. Christian, J. W., in *The Theory of Transformations in Metals and Alloys*. Pergamon Press, Oxford, 1975, p. 542.
77. Inoue, A. and Fan, C., *Mater. Trans. Japan. Inst. Metals*, 1999, **40**, 1376.
78. Zhang, T. and Inoue, A., *Mater. Trans. Japan. Inst. Metals*, to be submitted.
79. *Dunlop Catalog*, Tokyo, 1998.
80. Onugi, M., Inoue, A., Yamaguchi, T., Minamiguchi, H. and Iwata, K., *Materia Japan*, 1999, **38**, 251.